Cell

Grid Cells Use HCN1 Channels for Spatial Scaling

Lisa M. Giocomo,[1,*] Syed A. Hussaini,[2] Fan Zheng,[1] Eric R. Kandel,[2] May-Britt Moser,[1] and Edvard I. Moser[1,*]
[1]Kavli Institute for Systems Neuroscience and Centre for the Biology of Memory, Norwegian University of Science and Technology, 7030 Trondheim, Norway
[2]Department of Neuroscience, Kavli Institute for Brain Science and Howard Hughes Medical Institute, Columbia University, New York, NY 10032, USA
*Correspondence: lisa.m.giocomo@ntnu.no (L.M.G.), edvard.moser@ntnu.no (E.I.M.)
DOI 10.1016/j.cell.2011.08.051

SUMMARY

Entorhinal grid cells have periodic, hexagonally patterned firing locations that scale up progressively along the dorsal-ventral axis of medial entorhinal cortex. This topographic expansion corresponds with parallel changes in cellular properties dependent on the hyperpolarization-activated cation current (Ih), which is conducted by hyperpolarization-activated cyclic nucleotide-gated (HCN) channels. To test the hypothesis that grid scale is determined by Ih, we recorded grid cells in mice with forebrain-specific knockout of HCN1. We find that, although the dorsal-ventral gradient of the grid pattern was preserved in HCN1 knockout mice, the size and spacing of the grid fields, as well as the period of the accompanying theta modulation, was expanded at all dorsal-ventral levels. There was no change in theta modulation of simultaneously recorded entorhinal interneurons. These observations raise the possibility that, during self-motion-based navigation, Ih contributes to the gain of the transformation from movement signals to spatial firing fields.

INTRODUCTION

Grid cells in the medial entorhinal cortex (MEC) are place-modulated neurons with multiple firing fields covering the environment in a grid-like hexagonal array (Fyhn et al., 2004; Hafting et al., 2005). Several species have been reported to have grid cells, including mice (Fyhn et al., 2008), rats (Fyhn et al., 2004), bats (Yartsev et al., 2011), and humans (Doeller et al., 2010). Despite frequent variation in the animal's speed and direction, the firing locations of the grid cells remain rigidly periodic, pointing to the MEC circuit as a possible neural element for path integration-based spatial navigation (Hafting et al., 2005; McNaughton et al., 2006). Consistent with this possibility, the spatial phase offset of neighboring grid cells remains constant across environments, and grid cells preserve their periodic structure in complete darkness (Fyhn et al., 2007; Hafting et al., 2005). In all environments, the spatial scale of the grid cells is organized topographically along the dorsal-ventral axis of the MEC (Brun et al., 2008; Hafting et al., 2005; Sargolini et al., 2006). Grid scale is characterized by the size of the individual firing fields as well as the distance, or spacing, between the grid vertices. Both grid field size and grid spacing increase progressively from dorsal to ventral MEC.

The potential substrate underlying the topographical expansion of grid scale has remained unresolved. Grid patterns are thought to reflect the integration of position from instantaneous changes in the animal's velocity and direction (Burgess et al., 2007; Fuhs and Touretzky, 2006; McNaughton et al., 2006; O'Keefe and Burgess, 2005). If this is true, the incoming velocity signals themselves or the transformation of these inputs to spatial signals must be anatomically graded. Recent in vitro whole-cell patch-clamp studies have found several dorsal-ventral gradients in properties of entorhinal stellate cells that may be candidates for a differential transformation. Resonant properties of these cells, such as the membrane-potential oscillation frequency, change from high frequencies in the dorsal part of MEC to low frequencies in the ventral part (Giocomo and Hasselmo, 2008a; Giocomo et al., 2007; Heys et al., 2010). In addition, multiple temporal-integrative time constants of these cells increase from dorsal to ventral, such as the time constants of the excitatory postsynaptic potential (EPSP) and the spike after-hyperpolarization (Boehlen et al., 2010; Garden et al., 2008; Navratilova et al., 2011). These observations point to resonant and temporal-integrative properties of postsynaptic stellate cells as candidate mechanisms for graded transformation of velocity signals along the dorsal-ventral axis of MEC.

Resonance and temporal integration in entorhinal stellate cells share a common feature in their dependence on the hyperpolarization-activated cation current Ih, a current known to change topographically from dorsal to ventral MEC (Garden et al., 2008; Giocomo and Hasselmo, 2008b). Knockout of the hyperpolarization-activated cyclic nucleotide-gated 1 subunit (HCN1), which conducts Ih (Chen et al., 2001), slows down resonance and temporal summation in entorhinal layer II cells (Garden et al., 2008; Giocomo and Hasselmo, 2008b; Giocomo and Hasselmo, 2009). We used these physiological changes in HCN1 knockout mice to test the idea that changes in resonance or temporal summation determine grid scale in the MEC.

RESULTS

Experimental Groups, Tetrode Locations, and Histological Borders

To examine the contribution of h current-dependent single-cell properties to grid spacing, we recorded neural activity in the MEC of forebrain-restricted HCN1 knockout mice (KO) and matched littermate control mice (Nolan et al., 2004; Nolan et al., 2003) A total of 18 mice (8 KO and 10 control) were implanted with tetrodes aimed at MEC. The experimenters remained blind to the identity of the mouse group (KO versus control) until the data collection and preliminary analysis were completed.

We obtained data from a total of 965 well-separated cells in layers II and III of MEC (434 in KO and 531 in control). Cells from these two layers were distinguished by the denser staining in layer II compared to layer III. The border between MEC and other cortical regions was determined from Nissl-stained sagittal brain sections (Figure S1 available online) and based on Menno Witter's atlas for the hippocampal and parahippocampal cortex (Kjonigsen et al., 2011), as well as the Allen Brain Atlas. The average distance from the recording location to the dorsal border of MEC was 609 ± 16 μm in the KO group and 702 ± 10 μm in the control group (means ± SEM, range 1,000 and 1,100 μm, respectively; all data from the 100 cm box).

Behavioral Training

KO and control mice were trained to run randomly in a 100 × 100 cm or 50 × 50 cm open field. Trials lasted 20–40 min in the 100 cm box and 10–20 min in the 50 cm box, allowing the mouse enough time to cover the environment sufficiently. The 50 cm box provided sufficient conditions for identifying head direction and border cells, but the box was too small for visualizing the periodicity of grid fields at all dorsal-ventral MEC levels (Figure S2). Further analysis of grid cells was therefore carried out in the 100 cm box (333 cells in KO and 319 in control). On average, for trials with grid cells, HCN1 KO mice ran slightly faster than control mice (KO = 11.84 ± .21 cm/s, control = 9.57 ± .28 cm/s), but the speed difference did not affect the group difference in grid spacing (Figure S3).

HCN1 Knockout Does Not Change the Proportion of Grid Cells

Targeted mutation of HCN1 subunits did not reduce the number of grid cells. Grid cells were abundant in superficial layers of MEC (Figure 1). Spatial autocorrelation analysis confirmed the regularity and hexagonal pattern of the firing fields in these cells (Figures 1A and 1B). To estimate the proportion of grid cells, we performed a shuffling analysis on a cell-by-cell basis (Boccara et al., 2010; Langston et al., 2010). Grid cells were defined as cells with a grid score higher than the 99th percentile of shuffled data for the respective group, layer, and box size (Figures 1C and 1D). Using this criterion, in layers II and III of MEC we found 48 grid cells in control mice (15% of all cells) and 86 grid cells in KO mice (26% of all cells). The number of observed grid cells was significantly larger than expected by random selection from the shuffled distribution in both KO mice (layer II, Z = 42.88, $p < 0.001$; layer III, Z = 17.80, $p < 0.001$; binomial test with expected p value of 0.01) and control mice (layer II, Z = 21.95, $p < 0.001$; layer III, Z = 13.02, $p < 0.001$) (Figures 1C and 1D). There were significantly more grid cells in HCN1 KO compared to control (Z = 3.40, $p < 0.001$; layer II Z = .88, p = 39; layer III, Z = 2.53, $p < 0.05$; binomial test), but this was most likely due to uneven sampling within MEC across animals (Figure S4). There was no significant difference in the average firing rate of the grid cells in KO and control animals (2.09 ± .16 Hz and 2.16 ± .26 Hz, respectively; $t(132)$ = .34, p = 0.73) or in the magnitude of their periodicity (grid scores of .66 ± .03 and .71 ± .03, respectively; $t(132) = -1.04$, p = 0.30).

Increased Grid Scale in HCN1 KO Mice

Entorhinal cells in HCN1 KO mice had increased grid field size and grid spacing at all dorsal-ventral locations examined (Figures 2, 3, and 4). To estimate the impact of the loss of HCN1 subunits, we fit a linear regression line to scatterplots showing either grid spacing (Figure 2B) or grid field size (Figure 2C) as a function of dorsal-ventral position in MEC. Both regression lines had a significantly higher Y intercept in HCN1 KO mice than in control mice, as determined by an analysis of covariance (grid spacing: $F(1,124) = 83.71$, $\eta^2 = .40$, $p < 0.001$; grid field size: $F(1,130) = 68.97$, $\eta^2 = .35$, $p < 0.001$), suggesting that grid scale is increased after loss of HCN1. To compare the steepness of the dorsal-ventral gradient in grid scale, we next determined the slope of the regression lines for the two groups. In the HCN1 KO mice, the correlation with grid spacing was r (77) = .47 ($p < 0.001$; Figure 2B) and the correlation with field size was r (84) = .44 ($p < 0.001$; Figure 2C). In the control mice, the respective correlations were r (46) = .45 (p = 0.001; Figure 2B) and r (46) = .44 ($p < 0.01$; Figure 2C). The slope of the gradient in grid spacing was not significantly different between the two groups (grid spacing: $F(1,123) = 1.56$, $\eta^2 = .01$, p = 0.21; grid field size: $F(1,129) = 3.57$, $\eta^2 = .03$, p = 0.06). The ratio between grid spacing and grid field size (spacing/field size) did not differ significantly between control and KO mice (3.26 ± .07 and 3.32 ± .06, respectively, $t(124) = .68$, p = 0.50), indicating that spacing and size scaled up proportionately with loss of HCN1. Separate analysis of layer II cells gave an identical result (Y intercept for grid spacing: $F(1,91) = 81.68$, $\eta^2 = .47$, $p < 0.001$ and for grid field size: $F(1,95) = 69.01$, $\eta^2 = .42$, $p < 0.001$; slope for grid spacing: $F(1,90) = .07$, $\eta^2 = .001$, p = 0.79 and for grid field size: $F(1,94) = .87$, $\eta^2 = .01$, p = 0.35). The number of cells and the spatial range of dorsal-ventral locations were too small to conduct a similar analysis on grid cells in layer III. The significant increase in the Y intercept and the lack of change in the slope indicate that HCN1 plays a specific role in determining the range of the gradient in grid scale.

Interspike Interval and Theta Frequency

The increase in grid scale in HCN1 KO mice raises the possibility of an accompanying increase in the interspike interval. Because spike timing during theta oscillations may depend on intrinsic currents such as Ih (Hu et al., 2009; Hu et al., 2002; Navratilova et al., 2011), we analyzed the interspike interval for theta-modulated grid cells in HCN1 KO mice. Theta modulation of individual neurons was determined from the fast Fourier transform-based power spectrum of the spike train autocorrelation functions of the cells. A cell was defined as being theta modulated if the

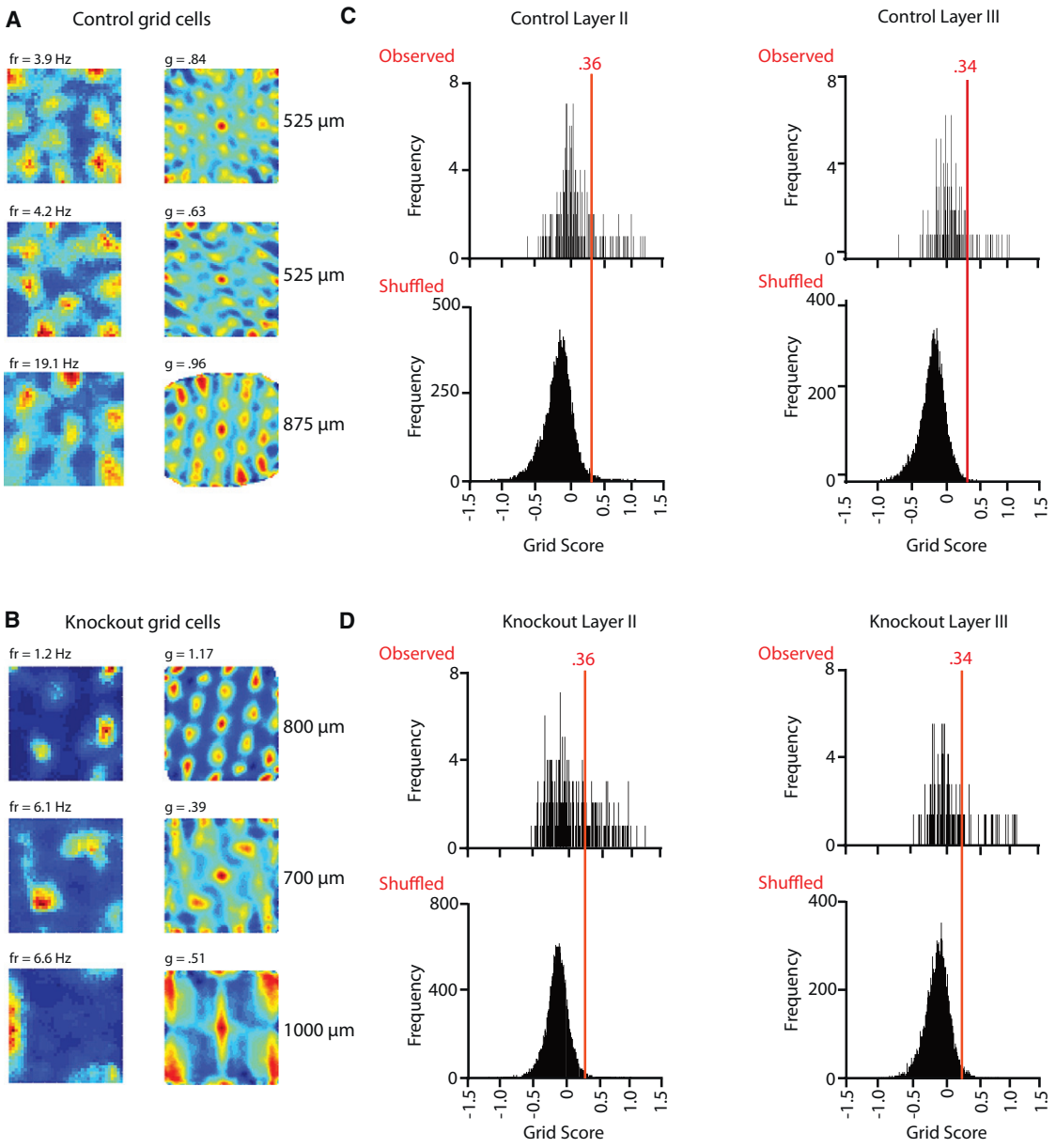

Figure 1. Examples of Grid Cells in Control Mice and HCN1 Knockout Mice

(A and B) Examples of grid cells in control mice (A) and HCN1 knockout mice (B). Three examples of grid cells from each group are shown. The mice walked in a 100 cm wide box. Rate maps (left column) and autocorrelation maps (right column) are color coded (dark blue, minimum rate; dark red, maximum rate). The scale of the autocorrelation diagrams is twice the scale of the rate maps. Maximum firing rate (fr) and grid score (g) are provided at the top of the plots. Distance from the dorsal entorhinal border (in µm) is marked on the right of each autocorrelation plot.

(C and D) Distribution of grid scores for cells in layer II (left) and layer III (right) in control (C) and knockout mice (D). Top rows show the distribution for values observed. Bottom rows show the distribution for randomly shuffled data, including all cells from the respective layer. For each trial of the shuffling procedure, the entire sequence of spikes fired by the cell was time-shifted along the rat's path by a semirandom interval, a rate map was generated, and a grid score was calculated. This procedure was repeated 100 times for each cell, yielding a total of 53,100 permutations for the 531 control neurons and 43,400 permutations for the 434 KO neurons. Red lines indicate the 99th percentile significance level for each shuffled distribution.

See Figure S7 for examples of acceptable clusters for shuffling analysis.

mean power within 1 Hz of each side of the peak in the 4–5 to 10–11 Hz frequency range was at least 3-fold greater than the mean spectral power between 0 Hz and 125 Hz. We observed theta modulation in 43.0% of grid cells in KO mice and 38.3% of grid cells in control mice. In grid cells, the interspike interval in the theta frequency range was significantly higher in KO mice than in control mice (control: 108.1 ± 2.4 ms, KO: 114.4 ± 1.6 ms; $t(53) = 2.28$, $p < 0.05$; Figure 5), indicating that larger grid spacing

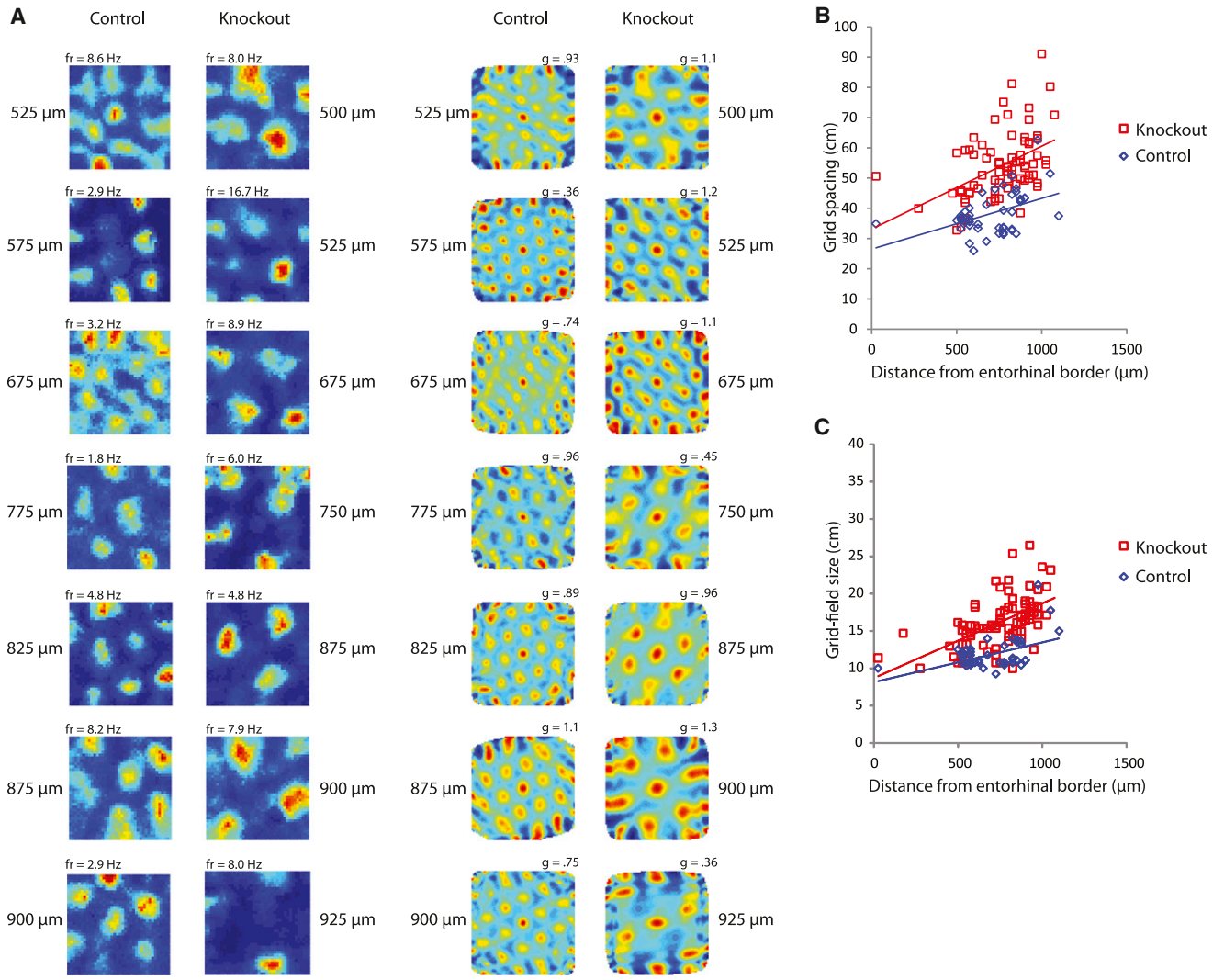

Figure 2. Increased Grid Scale in HCN1 Knockout Mice

(A) Seven grid cells recorded from control and knockout mice at increasing distance from the dorsal border of MEC. Left pair of columns shows rate maps; right pair shows autocorrelation maps for the same cells. Color coding as in Figures 1A and 1B. Maximum firing rate (fr) and grid score (g) are provided for each cell at the top of the plot. Distance from the dorsal entorhinal border (in µm) is marked to the side of each plot. Note that grid cell spacing is larger in HCN1 knockout mice than in control mice at all dorsal-ventral positions.

(B and C) Grid spacing (B) and grid field size (C) are significantly larger in HCN1 knockout mice than in controls. An increase in spacing and field size along the dorsal-ventral axis is observed in both groups. The analysis method for grid size sets a lower limit of 10 cm in field size, resulting in a slightly flatter slope in control mice compared to HCN1 knockout mice. The dorsal-ventral extent covered was not significantly different between HCN1 KO and control mice (751 ± 21 µm, 711 ± 26, respectively; t(132) = 1.17, p = 0.24).

See Figure S3 for more details.

occurred in conjunction with a lower "intrinsic firing" frequency. This difference was most pronounced at higher speeds (20–30 cm/s; control: 101.4 ± 2.4 ms, KO: 112.4 ± 2.0 ms, $t(53)$ = 2.53, $p < 0.05$; Figure 5B). The group difference in interspike intervals was observed only in principal cells; interspike intervals for theta-modulated entorhinal interneurons (71% of control and 79% of KO interneurons) were not different (control: 106.2 ± 2.3 ms, KO: 108.8 ± 3.3 ms; $t(36)$ = .59, p = 0.56; 20–30 cm/s: control: 99.5 ± 3.12 ms, KO: 102.9 ± 3.5 ms, $t(36)$ = .69, p = 0.50). The difference between principal cells and interneurons was not caused by differences in the size of the cell samples (55 versus 38 cells, respectively). The effect of sample size was addressed by repeated subsampling from the principal cell population, such that the number of cells (n = 38) was identical in the populations that were compared. Subsampling from the principal cell population yielded a larger effect size than in the interneuron population in 999 out of 1,000 permutations.

As expected, theta rhythmicity was observed in the local field potential in both control and KO mice. The power percentage of theta was numerically higher in KOs compared to control mice,

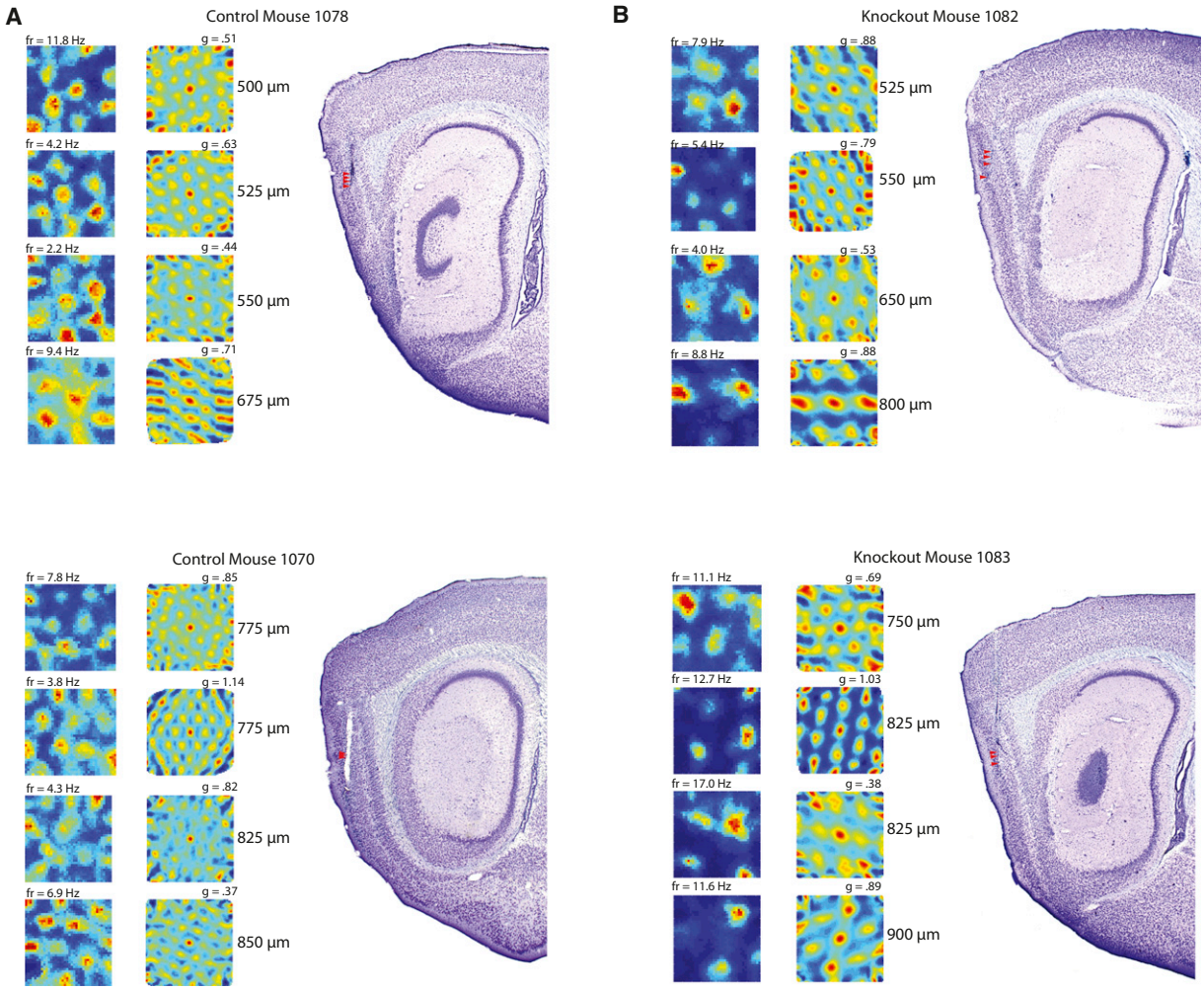

Figure 3. Examples of Grid Field Size and Grid Spacing from Individual Control and HCN1 Knockout Mice

(A and B) Four different grid cells recorded from two control (A) and two HCN1 knockout (B) mice. Symbols as in Figure 2. Firing rate plots (left columns) and autocorrelations (right columns) are shown for each animal. Histology showing the location of each example cell (red arrow) is shown on the right in each panel. Note that, at similar dorsal-ventral positions, grid cell spacing is larger in HCN1 knockout mice compared to control mice.
Histology for all mice is shown in Figure S1.

consistent with previous analysis of hippocampal theta in HCN1 KO mice (Nolan et al., 2004). The difference did not reach significance in the present study (466.7 ± 57.5 versus 319.2 ± 36.6, respectively; $t(132) = 1.79$, $p = 0.08$); however, the mean frequency of theta in the entorhinal EEG signal was higher in the control mice (8.63 ± .08 Hz and 8.25 ± .06 Hz, respectively; $t(81) = 3.85$, $p < 0.001$). The effect on theta frequency was modulated by running speed, but the modulation was stronger in control than in KO mice (slope of speed versus theta frequency relationship: $t(81) = 5.88$, $p < 0.001$; Figures 5C and S6). The reduced speed modulation, which coincides with the increase in grid spacing after loss of HCN1, is consistent with experimental work indicating a relationship between grid spacing and the degree of modulation by speed (Jeewajee et al., 2008). The reduction in the rate of increase in theta frequency with running speed additionally supports the idea that HCN1 channels contribute to setting the gain of velocity signals to the grid cells. Finally, the theta frequency in the local field potential was lower than the theta frequency of the discharge pattern in individual cells in both groups (differences of .60 ± .20 Hz and .46 ± .121 Hz, respectively; n = 53), indicating that phase precession mechanisms may be preserved in the HCN1 KO mice (O'Keefe and Recce, 1993).

Border Cells and Head Direction Cells

The proportion of entorhinal border cells and head direction cells (Sargolini et al., 2006; Solstad et al., 2008), as well as the properties of each cell type, should indicate whether knockout of HCN1 exclusively impacts the grid cell network or affects the spatial representation system more globally. Border cells fire at the highest rate when an animal is physically near one or multiple boundaries in the environment (e.g., the box walls), whereas

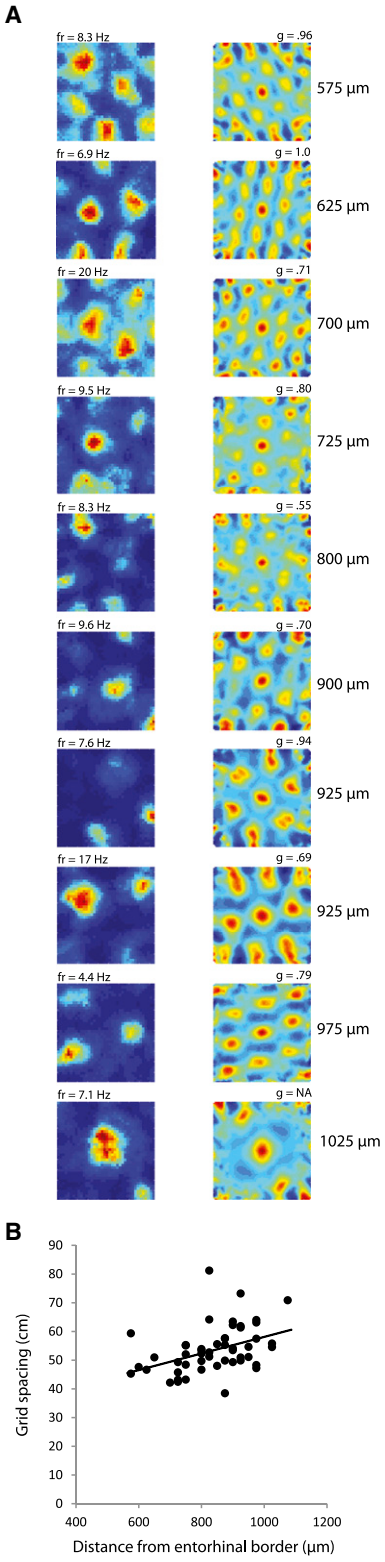

Figure 4. The Gradient in Grid Spacing along the Dorsal-Ventral Axis of a Single HCN1 Knockout Animal

(A) Examples of rate maps (left) and autocorrelation maps (right) for grid cells at increasing distance from the dorsal border of MEC. Symbols as in Figure 2. Note increasing grid spacing and field size along the dorsal-ventral axis.

(B) Scatterplot for grid spacing for all grid cells recorded in the same HCN1 knockout mouse.

See Figure S5 for possible cellular mechanisms contributing to the preserved gradient in grid spacing in HCN1 knockout mice.

head direction cells fire strongest when the animal's head is pointed in a particular direction. A cell was classified as a border cell or head direction cell if the border score for proximity to the walls or the length of the mean vector for directional tuning, respectively, was larger than the 99th percentile of the appropriate distribution of shuffled data generated from the entire set of cells recorded in the relevant brain region (Boccara et al., 2010). In control mice, we observed 24 border cells (7.5% of all cells) and 33 head direction cells (11.5% of all cells) in the 100 cm box. In HCN1 KO mice, we observed 38 border cells (11.4% of cells of all cells) and 92 head direction cells (29.4% of all cells). These numbers are significantly higher than expected by random selection from the shuffled distributions for border cells and for head direction cells (Figures 6 and 7). There was no significant difference in the number of border cells in HCN1 KO compared to control mice ($Z = -1.69$, $p = 0.09$; binomial test); however, there were significantly more head direction cells in HCN1 KO compared to control, probably due to uneven sampling within MEC in the two groups of animals ($Z = 5.39$, $p < 0.001$; binomial test; Figure S4).

Several properties of the border cells and head direction cells were similar between control and HCN1 KO mice. Average firing rate and directional modulation of border cells were not significantly different (firing rate = 2.11 ± .29 Hz and 2.81 ± .96 Hz, respectively; $t(60) = .84$, $p = 0.41$; mean vector length = .15 ± .02 and .14 ± .04, respectively; $t(53) = .41$, $p = 0.68$). Similarly, the sensitivity of head direction cells to direction, as determined by the length of the directional firing rate vector, was not significantly different between KOs and control mice (.27 ± .01 and .30 ± .01, respectively; $t(193) = 1.21$, $p = 0.23$).

Spatial Stability

Though the proportion of cell types remained unaltered in HCN1 KO mice, the spatial stability of grid and border cells was significantly elevated. Spatial stability was determined from correlations between rate maps for the first and second halves of the trial. Because stability can depend on the field size of grid cells, with larger grids prone to showing more stability than smaller grids, we fit a regression line for each group to scatterplots showing grid stability as a function of grid spacing. The regression line had a significantly higher Y intercept in HCN1 KO mice than in control mice [$F(1,122) = 43.22$, $\eta^2 = .26$, $p < 0.001$], indicating a general increase in grid cell stability in HCN1 KO mice. The spatial stability of border cells was also significantly higher in KO mice compared to controls (.40 ± .03 versus .27 ± .03, respectively; $t(87) = 2.72$, $p < 0.05$). Angular stability of head direction cells was not statistically different between HCN1 KO and control mice (67 ± .02 versus .61 ± .03; $t(193) = 1.70$, $p = 0.09$).

Previous reports indicate that HCN1 KO mice have enhanced spatial memory (Nolan et al., 2004), a puzzling result given the

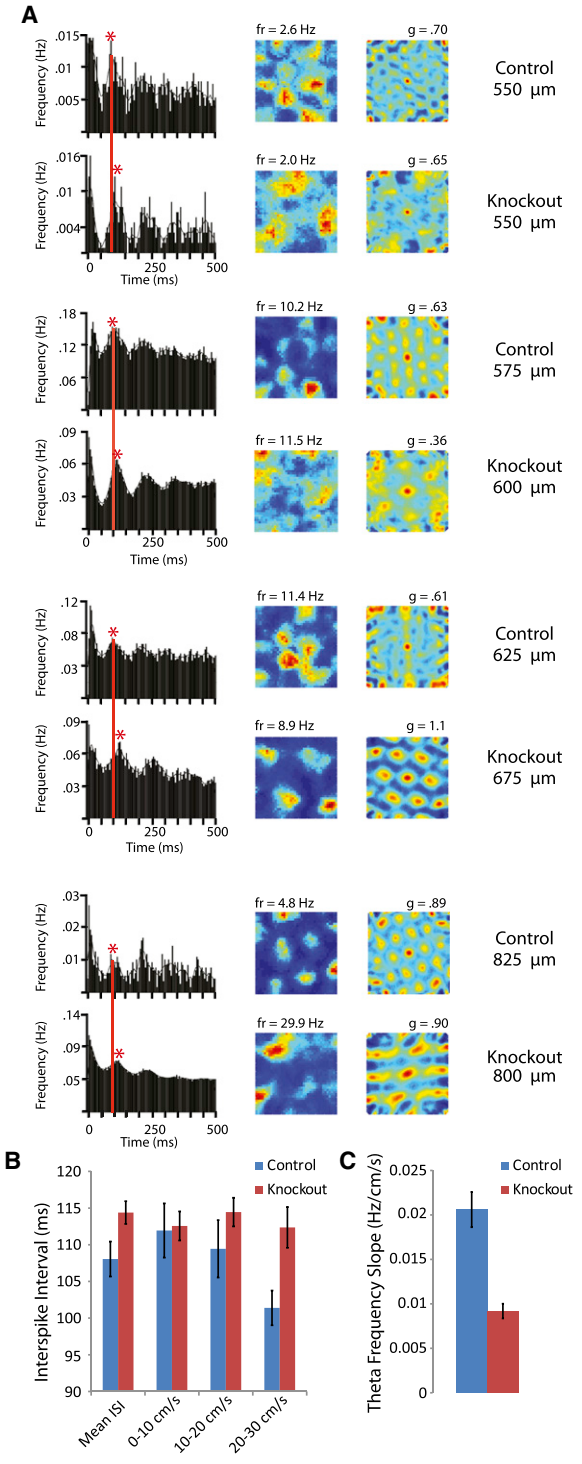

Figure 5. Increased Interspike Interval during Theta Activity in HCN1 Knockout Mice Compared to Control

(A) Examples of grid cells recorded in control mice and HCN1 knockout mice at similar distances from the dorsal border of MEC. One cell from each group is shown for each distance (top, control; bottom, knockout). (Left to right) Spike time autocorrelation diagrams, with a red line indicating the first peak in the control mouse diagram, rate map, and autocorrelation for the same cell. Symbols as in Figure 2.

(B) The interval between theta peaks was significantly larger in HCN1 knockout mice than in control mice (data are shown as mean ± SEM). Control mice showed a nonsignificant trend toward decreased values of the interspike interval with increasing speed, as determined by an analysis of covariance on speed and the interaction of speed by group (speed: $F(1,161) = 3.58$, $\eta^2 = .02$, $p = 0.06$; group × speed: $F(1,161) = 3.31$, $\eta^2 = .02$, $p = 0.07$).

(C) The theta frequency was significantly more modulated by running speed in control mice compared to KO mice. The mean slope (± SEM) of speed versus theta frequency relationship is shown for control and KO mice.

See Figure S6 for implications of theta oscillations on grid spacing.

potentially detrimental increase in grid scale in the same mouse strain. It is possible that HCN1 knockout aids learning by increasing the spatial stability of grid cells and border cells, leading to a more stable representation of the environment. This increase in spatial stability could result from the well-documented enhancement of long-term potentiation observed with HCN1 knockout (Nolan et al., 2004; Tsay et al., 2007).

DISCUSSION

The topographical organization of the grid cell network can be characterized by the slope of the dorsal-ventral gradient in grid spacing (slope), as well as the Y intercept of that gradient (ΔY). With loss of HCN1, we found a significant increase in the Y intercept, indicating that the electrophysiological properties of single neurons can strongly influence the scale of spatial representation. The increase in grid scale was accompanied by an increase in the interspike interval of theta modulated grid cells, suggesting that grid scale and theta frequency are mechanistically related. In contrast to the global shift in grid scale (ΔY), the steepness of the gradient (slope) remained unaffected. There was also no change in the theta period of entorhinal interneurons or in the proportion or properties of head direction cells and border cells.

The selective change in the Y intercept (ΔY) constrains the number of potential cellular mechanisms that could contribute to grid scale. Reducing Ih by knockout of HCN1 or pharmacological manipulation has differential effects on resonant and temporal-integrative gradients of entorhinal cells recorded in vitro (Figure S5). Knockout of HCN1 results in profound flattening of the dorsal-ventral gradient in resonance (Giocomo and Hasselmo, 2009), suggesting that the slope of that gradient depends almost exclusively on a gradient in the h current. The lack of a corresponding change in the slope of the gradient in grid scale indicates that the topographical expansion is not determined by HCN1-dependent resonance (Dodson et al., 2011). This has potential implications for a class of computational models termed "oscillatory interference models" (Blair et al., 2008; Burgess et al., 2007; Giocomo et al., 2007; O'Keefe and Burgess, 2005) in which the change in grid scale is generated by variations in the resonant frequency along the dorsal-ventral axis (Burgess, 2008; Giocomo et al., 2007; N. Burgess et al., 2005, Computational Cognitive Neuroscience, conference). The reduction in modulation of theta frequency by running speed seen with the loss of HCN1 is consistent with predictions made by some of these models (Burgess, 2008; Burgess et al., 2007). However, the pronouncedly slower oscillation observed

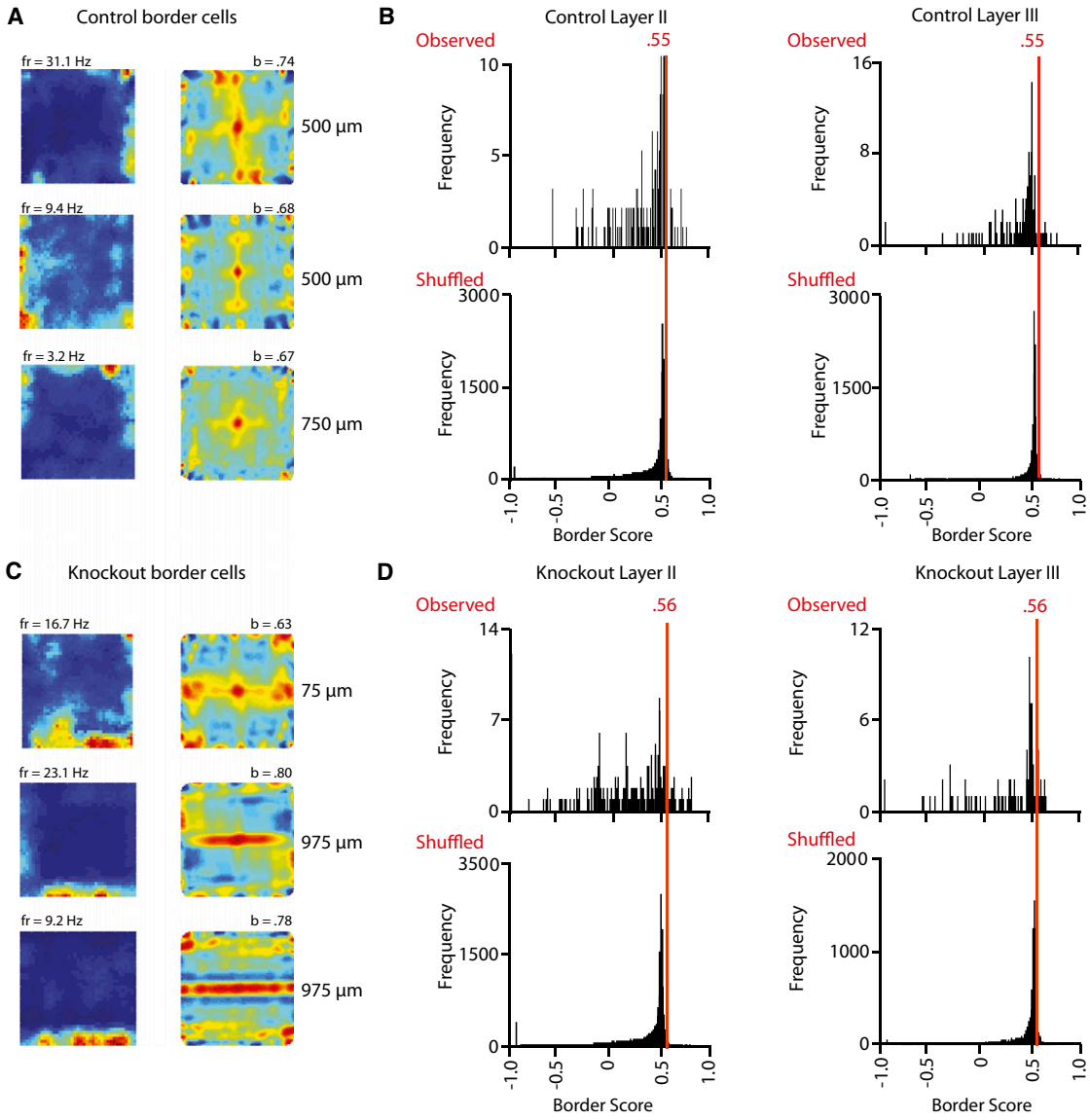

Figure 6. Border Cells Recorded from Control Mice and HCN1 Knockout Mice in the 100 cm Box

(A and C) Rate maps (left) and autocorrelation maps (right) for three representative border cells from each group. Symbols as in Figure 2. Border score (b) is provided at the top of the plots.

(B and D) Distribution of border scores for layer II (left) and layer III (right) cells in each group. Top rows show the distribution for values observed. Bottom rows show the distribution for randomly shuffled rate maps for all cells from the respective layer. Red lines indicate the 99th percentile significance level for each shuffled distribution. Border cell numbers were significantly higher than expected by random selection from the shuffled distribution for border cells (CON layer II, $Z = 9.99$, $p < 0.001$; CON layer III, $Z = 6.33$, $p < 0.001$; KO layer II, $Z = 15.71$, $p < 0.001$; KO layer III, $Z = 10.86$, $p < 0.001$).

Data for the 50 cm box are shown in Figure S2.

in vitro with loss of HCN1 predicts an increase in grid cell spacing that is far larger than what we observed in vivo in the present data (see Figure S6 for further discussion). Additional experiments are needed to determine: (1) whether grid spacing might be correlated with resonant currents, such as the M current (Heys et al., 2010; Hu et al., 2009; Hu et al., 2002; Kispersky et al., 2010), that might be activated at more depolarized membrane potentials than those investigated in the HCN1 knockout mice, or (2) whether the grid spacing is maintained by residual Ih, conducted by HCN2 subunits (Giocomo and Hasselmo, 2009; Heys et al., 2010; Hu et al., 2002, 2009; Kispersky et al., 2010; Nolan et al., 2007).

Whereas the dorsal-ventral gradient in resonant properties depends quite exclusively on HCN1, the gradient in temporal-integrative properties depends on a gradient in both the h current and the leak K+ current (Garden et al., 2008). A reduction of Ih increases the time constant of temporal summation across the entire dorsal-ventral axis (Garden et al., 2008;

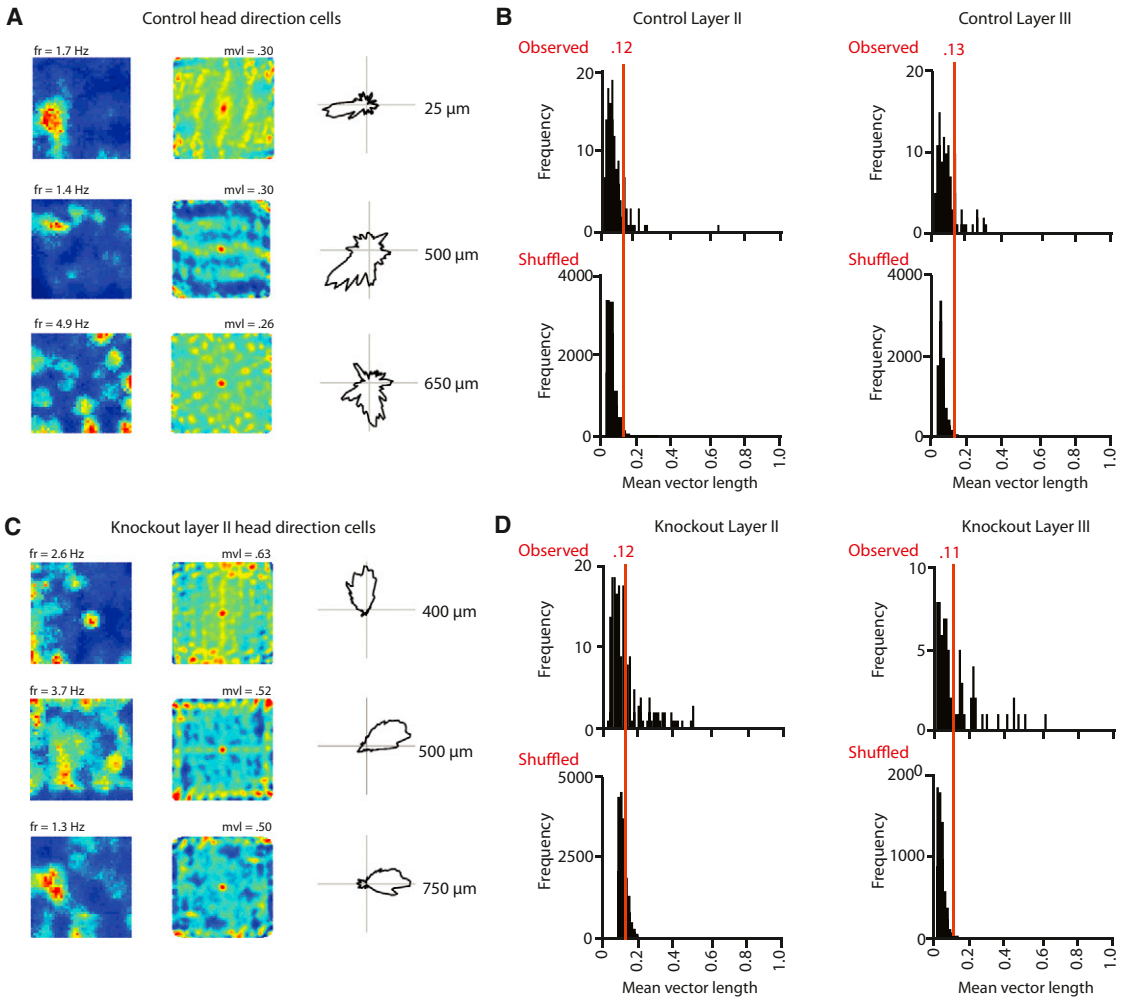

Figure 7. Head Direction Cells Recorded from Control Mice and HCN1 Knockout Mice in the 100 cm Box

(A and C) Three examples of head direction cells from each group are shown (left, rate map; middle, autocorrelation map, right direction map). Symbols as in Figure 2. The directional plots show firing rate as a function of head direction.

(B and D) Distribution of mean vector length for layer II (left) and layer III (right) cells in knockout mice in the 100 cm box. Top rows show the distribution for values observed. Bottom rows show the distribution for randomly shuffled rate maps for all cells from the respective layer. Red lines indicate the 99th percentile significance level for each shuffled distribution. Head direction cell numbers were significantly higher than expected by random selection from the shuffled distribution for head direction cells (CON layer II, $Z = 10.6$, $p < 0.001$; CON layer III, $Z = 15.0$, $p < 0.001$; KO layer II, $Z = 40.6$, $p < 0.001$; KO layer III, $Z = 30.3$, $p < 0.001$).

Proportions for all cells are shown in Figure S4.

Giocomo & Hasselmo, 2009). This change in Y intercept, but not slope, generates the prediction that, if temporal summation is critical for grid scale, we should observe a shift in the Y intercept but no change in the slope of the dorsal-ventral gradient for grid scale in HCN1 KO mice. This is exactly what we observed. The findings thus point to slower temporal-integrative properties as a possible cause of the global shift in grid scale (Dodson et al., 2011).

The entorhinal cortex is an important element of a path integration network in which position is computed from changes in the animal's angular and linear velocity (McNaughton et al., 2006). The topographical expansion of the grid representation raises the possibility that either the velocity signal or the transformation of such a signal is graded along the dorsal-ventral axis of MEC (Maurer et al., 2005; McNaughton et al., 2006; O'Keefe and Burgess, 2005). This hypothesis receives support from the observation that, in the entorhinal cortex, increases in grid spacing are accompanied by a decrease in the amount that speed affects theta frequency (Jeewajee et al., 2008). The present study, together with previous intracellular recordings in vitro, identifies variations in temporal integration properties as a candidate for differential translation of velocity signals. Such a role could be performed in several ways. First, the time constant of synaptic potentials, or the total conductance value of the neuron, could be used to determine the spatial tuning of phase to rate code transformations (Burgess, 2008;

Dodson et al., 2011; Zilli and Hasselmo, 2010). Loss of Ih by knockout of HCN1 causes an increase in the time constants of synaptic integration due to a decrease in Ih conductance (Garden et al., 2008; Giocomo and Hasselmo, 2009), both of which could increase the grid field size or spacing. Alternatively, a gradient in the time constant of the action potential after hyperpolarization (AHP) could structure a topographical attenuation of velocity-dependent signals by gradually increasing, along the dorsal-ventral axis, the time window for reinitiation of network activity at the start of each theta cycle (Navratilova et al., 2011). The consequence would be an increase in the scale of the grid. Consistent with this possibility, loss of HCN1 increases the time constant of the AHP (Nolan et al., 2007).

Our findings identify HCN1-expressing channels as strong determinants of spatial scale in the MEC. The increase occurs complementary to an increase in the size of place fields in the hippocampus (Hussaini et al., 2011), indicating that common mechanisms might be involved in setting the scales of grid cells and place cells. Whether these effects are induced locally remains to be determined. In principle, the scale change could result from the loss of HCN1 in regions upstream of the entorhinal and hippocampal regions. One possible site of action is the medial septum, which provides theta-patterned input to both the MEC and the hippocampus. The subtle drop in the frequency of field theta oscillations (.38 Hz) in the KO mice is consistent with some contribution of the medial septum; however, the fact that the subunit with the highest expression in medial septum is HCN2 (Santoro et al., 2000), which was preserved in our KO animals, speaks against a major influence. Our comparison of entorhinal principal cells and interneurons may be informative about the specific site of action. Interneurons lack well-defined firing fields, but their theta-modulated firing patterns make it possible to estimate the effect of HCN1 on temporal periodicity, which, in the principal cells, scaled up in parallel with spatial periodicity. With an external site of action, such as the hippocampus, we would expect the temporal-spatial scale change to be expressed throughout the entorhinal network and in all cells influenced by the external signal, irrespective of whether they express HCN1 channels or not. Our observations showed a selective change in the principal cell population, consistent with the observation that Ih is not expressed in major interneuron subtypes of the MEC (B. Tahvildari et al., 2009, Soc. Neurosci., abstract) and consistent with a direct action of HCN1 in the stellate cells of the MEC.

EXPERIMENTAL PROCEDURES

Subjects

Neural activity was recorded in MEC in 18 freely moving male mice. Ten of these mice were littermate wild-type control mice, and eight were forebrain-restricted KO mice (Nolan et al., 2003). Forebrain-restricted mice were bred at Columbia University as described previously (Nolan et al., 2003, 2004). Mice were generated from a hybrid 50:50% C57BL/6J:129SVEV background.

Surgery

The mice were implanted in one hemisphere with an eight-channel microdrive connected to two tetrodes cut flat at the same level. The tetrodes were made of 17 μm polyimide-coated platinum-iridium (90%–10%) wire. The electrode tips had been platinum plated to reduce electrode impedances to 200 kΩ at 1 kHz. The tetrode bundle was implanted at AP .3–.5 mm in front of the transverse sinus, 3.1–3.25 mm from the midline, and .8–1.0 mm below the dura. The implants were angled 5–8 degrees in the posterior direction in the sagittal plane.

Data Collection

From 3 days after implantation, the mice were exposed to two black square enclosures (50 × 50 × 50 cm or 100 × 100 × 50 cm). Recorded signals were amplified 8,000 to 25,000 times and band pass filtered between 0.8 and 6.7 kHz. Triggered spikes were stored to a disk at 48 kHz (50 samples per waveform, 8 bits/sample) with a 32 bit time stamp (clock rate at 96 kHz). EEG was recorded single ended from one of the electrodes. The EEG was amplified 3,000–10,000 times, lowpass filtered at 500 Hz, sampled at 4,800 Hz, and stored with the unit data. The recording system tracked the position of two light-emitting diodes (LEDs), one large and one small, on the head stage (sampling rate 50 Hz) by means of an overhead video camera.

Spike Sorting and Cell Classification

Spike sorting was performed offline using graphical cluster-cutting software. Clustering was performed manually in two-dimensional projections of the multidimensional parameter space (consisting of waveform amplitudes), using autocorrelation and crosscorrelation functions as additional separation tools (Figure S7). Putative excitatory cells were distinguished from putative interneurons (Figure S7). Cluster separation was estimated by calculating distances, in Maholonobis space, between clustered spikes from different cells on the same tetrode (isolation distances) (Schmitzer-Torbert et al., 2005) (Figure S7).

Position Estimate

Position estimates were based on tracking of the LEDs on the head stage connected to the microdrive. To characterize firing fields, we sorted the position data into 2.5 cm × 2.5 cm bins and smoothed the path with a 21 sample boxcar window filter (400 ms, ten samples on each side). Maps for number of spikes and time were smoothed individually using a quasi-Gaussian kernel over the surrounding 5 × 5 bins (Langston et al., 2010). Firing rates were determined by dividing spike number and time for each bin of the two smoothed maps. The peak rate was defined as the rate in the bin with the highest rate in the firing rate map.

Analysis of Grid Cells

The structure of the rate maps was evaluated for all cells with more than 100 spikes by calculating the spatial autocorrelation for each smoothed rate map. The degree of spatial periodicity (gridness or grid scores) was determined for each recorded cell by taking a circular sample of the autocorrelogram, centered on the central peak but with the central peak excluded, and comparing rotated versions of this sample (Langston et al., 2010; Sargolini et al., 2006). Grid cells were defined as cells in which rotational symmetry-based grid scores exceeded the 99th percentile of a distribution of grid scores for shuffled recordings from the entire population of cells in the same age group and the same brain region. Shuffling was performed in the same way as by Langston et al. (2010) and is described in the Extended Experimental Procedures. Grid spacing was defined as the median distance between the center and the nearest six peaks in the autocorrelogram. Because of the sensitivity of the analysis to noise in the grid autocorrelations, grid spacing was analyzed only for cells in which the median distance to the six nearest peaks matched the radius of the circle that gave the highest grid score (the "outer radius" [OR]). When the ratio between these two measures was beyond 2 SD of the mean (mean ratio 1.26, SD 0.32), the cell was excluded (7 out of 134 cells, all of which had noisy grids). Grid field size was defined as the radius of the circle around the center field of the autocorrelation map, referred to as the "inner radius" (IR).

Analysis of Border Cells

Border cells were identified by computing, for each cell, the difference between the maximal length of a wall touching on any single firing field of the cell and the average distance of the field from the nearest wall, divided

by the sum of those values (Solstad et al., 2008). Firing fields were defined as collections of neighboring pixels with firing rates 0.3-fold higher than the cell's peak firing rate that cover a total area of at least 200 cm^2. Border cells were defined as cells with border scores significantly exceeding the degree of wall-related firing that would be expected by chance. The significance level was determined for each group, cell layer, and box size by a shuffling procedure performed for experiments in the square boxes in the same way as for grid cells. Cells were defined as being border cells if the border score from the recorded data was higher than the 99th percentile for border scores in the distribution generated from the shuffled data. If a cell was recorded in the 50 cm box and 100 cm box, the session in the 100 cm box was used for analysis of spatial stability.

Analysis of Head Direction Cells

Directional analyses were only performed for experiments with two LEDs. The mouse's head direction was calculated for each tracker sample from the projection of the relative position of the two LEDs onto the horizontal plane. Some early sessions were recorded using only one diode, so the entire set of cells analyzed for head direction (463 control cells and 368 KO cells) was slightly smaller than the set analyzed for grid cells and border cells. The directional tuning function for each cell was obtained by plotting the firing rate as a function of the mouse's directional heading, divided into bins of 3 degrees and smoothed with a 14.5 degree mean window filter (14 bins on each side). The strength of directional tuning was estimated by computing the length of the mean vector for the circular distribution of firing rate. Head direction-modulated cells were defined as cells with mean vector lengths significantly exceeding the degree of directional tuning that would be expected by chance. The significance level was determined by each group, cell layer, and box size by a shuffling procedure performed for experiments in the square boxes in the same way as for grid cells. Cells were defined as directionally modulated if the mean vector from the recorded data was longer than the 99th percentile of mean vector lengths in the distribution generated from the shuffled data. If a cell was recorded in the 50 cm box and 100 cm box, the session in the 100 cm box was used for analysis of spatial stability.

Theta Rhythm and Theta Modulation

To estimate variations in neural activity across the theta cycle, we filtered local EEG offline, as described previously (Langston et al., 2010). For the filtering, 4 and 5 Hz were chosen as stopband and passband frequencies, respectively, at the low-end cut-off; 10 and 11 Hz were chosen as passband and stopband high cut-off frequencies. Theta modulation of individual neurons was determined from the fast Fourier transform-based power spectrum of the spike train autocorrelation functions of the cells. A cell was defined as being theta modulated if the mean power within 1 Hz of each side of the peak in the 4–5 to 10–11 Hz frequency range was at least 3-fold greater than the mean spectral power between 0 Hz and 125 Hz.

Spatial Stability

Spatial stability was determined from the spatial correlation estimated for each cell by correlating the rates of firing in corresponding bins of the pair of smoothed rate maps. Within trial stability was estimated by computing spatial correlations between rate maps for the first and second halves of the trial.

Histology and Reconstruction of Recording Positions

Electrodes were not moved after the final recording session. The mice were killed with an overdose of Equithesin and were transcardially perfused with 0.9% saline (wt/vol) followed by 4% formaldehyde (wt/vol). The brains were extracted and stored in 4% formaldehyde. At least 24 hr later, the brains were quickly frozen, cut in sagittal sections (30 μm) using a cryostat, mounted, and stained with cresyl violet. The positions of the tips of the recording electrodes were determined from digital pictures of the brain sections. The measurements were made using AxioVision (LE Rel. 4.3). The laminar location of the recording electrodes in MEC was determined on the basis of cytoarchitectonic criteria.

Statistical Analysis

To compare the slope and Y intercept of gradients in spatial properties of grid and border cells, we ran a univariate analysis of covariance (ANCOVA) in SPSS. First, we tested the data for an interaction between the main factors to determine whether the regression lines for control and knockout mice showed significantly different slopes. Next, to test for a significant difference in the Y intercept, we used the presence or absence of a significant slope difference to set up the ANCOVA model. If no significant difference in slope was detected, the ANCOVA was run without an interaction term, thus making the assumption of equal slope values for the two groups. If a significant difference in slope was detected, the analysis was run with the interaction term, thus making the assumption of unequal slope values for the two groups. p values below 0.05 were considered significant. Effect size is reported as η^2.

SUPPLEMENTAL INFORMATION

Supplemental Information includes Extended Experimental Procedures and seven figures and can be found with this article online at doi:10.1016/j.cell.2011.08.051.

ACKNOWLEDGMENTS

We thank R. Skjerpeng for programming; Ø. Salvesen for statistical advice; A.M. Amundsgård, I. Hammer, K. Haugen, and H. Waade for technical assistance; and M.E. Hasselmo, T. Solstad, and J.F. Storm for helpful discussion and/or comments on the manuscript. This work was supported by a Marie Curie Fellowship to L.M.G. from the European Commission; an Advanced Investigator Grant to E.I.M. from the European Research Council; an NIH grant MH080745 to S.A.H. and E.R.K.; the Howard Hughes Medical Institute (E.R.K.); the Kavli Foundation (M.-B.M. and E.I.M.); and a Centre of Excellence grant from the Norwegian Research Council (M.-B.M. and E.I.M.).

L.M.G., M.-B.M., and E.I.M. planned experiments and analyses. S.A.H. and E.R.K. generated the mice. L.M.G. collected data with help from S.A.H. and F.Z. L.M.G. analyzed the data, and L.M.G. wrote the paper with help from E.I.M. and M.-B.M. All authors contributed to discussion.

Received: January 21, 2011
Revised: June 28, 2011
Accepted: August 15, 2011
Published online: November 17, 2011

REFERENCES

Blair, H.T., Gupta, K., and Zhang, K. (2008). Conversion of a phase- to a rate-coded position signal by a three-stage model of theta cells, grid cells, and place cells. Hippocampus *18*, 1239–1255.

Boccara, C.N., Sargolini, F., Thoresen, V.H., Solstad, T., Witter, M.P., Moser, E.I., and Moser, M.B. (2010). Grid cells in pre- and parasubiculum. Nat. Neurosci. *13*, 987–994.

Boehlen, A., Heinemann, U., and Erchova, I. (2010). The range of intrinsic frequencies represented by medial entorhinal cortex stellate cells extends with age. J. Neurosci. *30*, 4585–4589.

Brun, V.H., Solstad, T., Kjelstrup, K.B., Fyhn, M., Witter, M.P., Moser, E.I., and Moser, M.B. (2008). Progressive increase in grid scale from dorsal to ventral medial entorhinal cortex. Hippocampus *18*, 1200–1212.

Burgess, N. (2008). Grid cells and theta as oscillatory interference: theory and predictions. Hippocampus *18*, 1157–1174.

Burgess, N., Barry, C., and O'Keefe, J. (2007). An oscillatory interference model of grid cell firing. Hippocampus *17*, 801–812.

Chen, S., Wang, J., and Siegelbaum, S.A. (2001). Properties of hyperpolarization-activated pacemaker current defined by coassembly of HCN1 and HCN2 subunits and basal modulation by cyclic nucleotide. J. Gen. Physiol. *117*, 491–504.

Dodson, P.D., Pastoll, H., and Nolan, M.F. (2011). Dorsal-ventral organization of theta-like activity intrinsic to entorhinal stellate neurons is mediated by differences in stochastic current fluctuations. J. Physiol. *589*, 2993–3008.

Doeller, C.F., Barry, C., and Burgess, N. (2010). Evidence for grid cells in a human memory network. Nature *463*, 657–661.

Fuhs, M.C., and Touretzky, D.S. (2006). A spin glass model of path integration in rat medial entorhinal cortex. J. Neurosci. *26*, 4266–4276.

Fyhn, M., Hafting, T., Witter, M.P., Moser, E.I., and Moser, M.B. (2008). Grid cells in mice. Hippocampus *18*, 1230–1238.

Fyhn, M., Molden, S., Witter, M.P., Moser, E.I., and Moser, M.B. (2004). Spatial representation in the entorhinal cortex. Science *305*, 1258–1264.

Fyhn, M.H., Hafting, T.F., Treves, A., Moser, M.B., and Moser, E.I. (2007). Hippocampal remapping and grid realignment in entorhinal cortex. Nature *446*, 190–194.

Garden, D.L., Dodson, P.D., O'Donnell, C., White, M.D., and Nolan, M.F. (2008). Tuning of synaptic integration in the medial entorhinal cortex to the organization of grid cell firing fields. Neuron *60*, 875–889.

Giocomo, L.M., and Hasselmo, M.E. (2008a). Computation by oscillations: implications of experimental data for theoretical models of grid cells. Hippocampus *18*, 1186–1199.

Giocomo, L.M., and Hasselmo, M.E. (2008b). Time constants of h current in layer ii stellate cells differ along the dorsal to ventral axis of medial entorhinal cortex. J. Neurosci. *28*, 9414–9425.

Giocomo, L.M., and Hasselmo, M.E. (2009). Knock-out of HCN1 subunit flattens dorsal-ventral frequency gradient of medial entorhinal neurons in adult mice. J. Neurosci. *29*, 7625–7630.

Giocomo, L.M., Zilli, E.A., Fransén, E., and Hasselmo, M.E. (2007). Temporal frequency of subthreshold oscillations scales with entorhinal grid cell field spacing. Science *315*, 1719–1722.

Hafting, T., Fyhn, M., Molden, S., Moser, M.B., and Moser, E.I. (2005). Microstructure of a spatial map in the entorhinal cortex. Nature *436*, 801–806.

Heys, J.G., Giocomo, L.M., and Hasselmo, M.E. (2010). Cholinergic modulation of the resonance properties of stellate cells in layer II of medial entorhinal cortex. J. Neurophysiol. *104*, 258–270.

Hu, H., Vervaeke, K., Graham, L.J., and Storm, J.F. (2009). Complementary theta resonance filtering by two spatially segregated mechanisms in CA1 hippocampal pyramidal neurons. J. Neurosci. *29*, 14472–14483.

Hu, H., Vervaeke, K., and Storm, J.F. (2002). Two forms of electrical resonance at theta frequencies, generated by M-current, h-current and persistent Na+ current in rat hippocampal pyramidal cells. J. Physiol. *545*, 783–805.

Hussaini, S.A., Kempadoo, K.A., Thuault, S.J., Siegelbaum, S.A., and Kandel, E.R. (2011). Increased size and stability of CA1 and CA3 place fields in HCN1 knockout mice. Neuron *72*, 643–653.

Jeewajee, A., Barry, C., O'Keefe, J., and Burgess, N. (2008). Grid cells and theta as oscillatory interference: electrophysiological data from freely moving rats. Hippocampus *18*, 1175–1185.

Kispersky, T., White, J.A., and Rotstein, H.G. (2010). The mechanism of abrupt transition between theta and hyper-excitable spiking activity in medial entorhinal cortex layer II stellate cells. PLoS ONE *5*, e13697.

Kjonigsen, L.J., Leergaard, T.B., Witter, M.P., and Bjaalie, J.G. (2011). Digital atlas of anatomical subdivisions and boundaries of the rat hippocampal region. Front. Neuroinform. *5*, 2.

Langston, R.F., Ainge, J.A., Couey, J.J., Canto, C.B., Bjerknes, T.L., Witter, M.P., Moser, E.I., and Moser, M.B. (2010). Development of the spatial representation system in the rat. Science *328*, 1576–1580.

Maurer, A.P., Vanrhoads, S.R., Sutherland, G.R., Lipa, P., and McNaughton, B.L. (2005). Self-motion and the origin of differential spatial scaling along the septo-temporal axis of the hippocampus. Hippocampus *15*, 841–852.

McNaughton, B.L., Battaglia, F.P., Jensen, O., Moser, E.I., and Moser, M.B. (2006). Path integration and the neural basis of the 'cognitive map'. Nat. Rev. Neurosci. *7*, 663–678.

Navratilova, Z., Giocomo, L.M., Fellous, J.M., Hasselmo, M.E., and McNaughton, B.L. (2011). Phase precession and variable spatial scaling in a periodic attractor map model of medial entorhinal grid cells with realistic after-spike dynamics. Hippocampus, in press.

Nolan, M.F., Dudman, J.T., Dodson, P.D., and Santoro, B. (2007). HCN1 channels control resting and active integrative properties of stellate cells from layer II of the entorhinal cortex. J. Neurosci. *27*, 12440–12451.

Nolan, M.F., Malleret, G., Dudman, J.T., Buhl, D.L., Santoro, B., Gibbs, E., Vronskaya, S., Buzsáki, G., Siegelbaum, S.A., Kandel, E.R., and Morozov, A. (2004). A behavioral role for dendritic integration: HCN1 channels constrain spatial memory and plasticity at inputs to distal dendrites of CA1 pyramidal neurons. Cell *119*, 719–732.

Nolan, M.F., Malleret, G., Lee, K.H., Gibbs, E., Dudman, J.T., Santoro, B., Yin, D., Thompson, R.F., Siegelbaum, S.A., Kandel, E.R., and Morozov, A. (2003). The hyperpolarization-activated HCN1 channel is important for motor learning and neuronal integration by cerebellar Purkinje cells. Cell *115*, 551–564.

O'Keefe, J., and Burgess, N. (2005). Dual phase and rate coding in hippocampal place cells: theoretical significance and relationship to entorhinal grid cells. Hippocampus *15*, 853–866.

O'Keefe, J., and Recce, M.L. (1993). Phase relationship between hippocampal place units and the EEG theta rhythm. Hippocampus *3*, 317–330.

Santoro, B., Chen, S., Luthi, A., Pavlidis, P., Shumyatsky, G.P., Tibbs, G.R., and Siegelbaum, S.A. (2000). Molecular and functional heterogeneity of hyperpolarization-activated pacemaker channels in the mouse CNS. J. Neurosci. *20*, 5264–5275.

Sargolini, F., Fyhn, M., Hafting, T., McNaughton, B.L., Witter, M.P., Moser, M.B., and Moser, E.I. (2006). Conjunctive representation of position, direction, and velocity in entorhinal cortex. Science *312*, 758–762.

Schmitzer-Torbert, N., Jackson, J., Henze, D., Harris, K., and Redish, A.D. (2005). Quantitative measures of cluster quality for use in extracellular recordings. Neuroscience *131*, 1–11.

Solstad, T., Boccara, C.N., Kropff, E., Moser, M.B., and Moser, E.I. (2008). Representation of geometric borders in the entorhinal cortex. Science *322*, 1865–1868.

Tsay, D., Dudman, J.T., and Siegelbaum, S.A. (2007). HCN1 channels constrain synaptically evoked Ca2+ spikes in distal dendrites of CA1 pyramidal neurons. Neuron *56*, 1076–1089.

Yartsev, M.M., Witter, M.P., and Ulanovsky, N. (2011). Grid cells without theta oscillations in the entorhinal cortex of bats. Nature *479*, 103–107.

Zilli, E.A., and Hasselmo, M.E. (2010). Coupled noisy spiking neurons as velocity-controlled oscillators in a model of grid cell spatial firing. J. Neurosci. *30*, 13850–13860.

Cell

EXTENDED EXPERIMENTAL PROCEDURES

Subjects

The generation of the forebrain restricted mice was initially described and published in Nolan et al., 2003. The HCN1 gene was inactivated by deleting the exon encoding the P region and S6 transmembrane domain. Conditional and conventional knockouts were generated using the three loxP site strategy. Forebrain restriction of the HCN1 deletion was obtained by crossing transgenic mice expressing Cre-recombinase under the control of the CaMKIIα-promoter with the floxed animals to generate HCN1$^{f/f,cre}$ mice. The mice were shipped to the Norwegian University of Science and Technology at 3-6 months of age where they rested from 2 weeks to 6 months before surgery. Implanted mice were allowed free access to food and water for 1 week after surgery, after which they were mildly food deprived to motivate exploratory behavior.

Surgery

Until surgery, the animals were housed together with their littermates in transparent cages. Mice ranged from 6 months to 1 year of age at the time of surgery. On the day of surgery, the mice were anesthetized with a mixture of pentobarbital and choral hydrate (Equithesin; .12 ml/30 g). Levels of anesthesia were monitored regularly by testing toe and tail pinch reflexes. The mice were implanted in one hemisphere with an 8-channel microdrive connected to 2 tetrodes cut flat at the same level. A jeweler's screw fixed to the skull served as the ground electrode. The microdrive was secured to the skull using small watchmaker's screws and dental cement. Following recovery of reflexes after anesthesia, the mice were returned to the housing room. After surgery, the mice were housed individually in transparent plexiglass cages in a temperature and humidity controlled vivarium near the recording room. All mice were maintained on a 12 hr light/ 12 hr dark schedule. Testing occurred in the dark phase.

Data Collection

Behavioral training started 3 days after the surgery and data collection started 1 week after the surgery. Before each recording trial, the mouse rested on a towel in a large transparent box on a pedestal. While the mouse was resting in the transparent box, the tetrodes were lowered in steps of 25 μm, up to 50 μm in a single day, until single neurons were isolated at the appropriate depth. The mouse was connected to the recording equipment via AC-coupled unity-gain operational amplifiers close to the mouse's head, using a lightweight counterbalanced cable that allowed the animal to move freely in the transparent box and the recording boxes. When the spike amplitudes exceeded 2 times the noise level (r.m.s. 20-30 μV) the mouse was placed individually into the test box and neural activity was recorded during spontaneous exploratory food-motivated running. After each finished set of experiments, the tetrodes were moved further (25 μm) until new well-separated cells were encountered. The recording system tracked the position of two light emitting diodes (LEDs), one large and one small, on the head stage (sampling rate 50 Hz) by means of an overhead video camera. The LEDs were separated by 5-7 cm and aligned with the body axis of the mouse.

Apparatus and Training Procedures

The walls of both enclosures (50 × 50 × 50 cm or 100 × 100 × 50 cm) were covered with black adhesive plastic and a polarizing white cue card (20 cm × 50 cm) was displayed in a constant location midway between the corners of one of the walls. Running was maintained with small food rewards (crumbled vanilla biscuits) that were scattered around the enclosure to encourage foraging. The box was surrounded by curtains. Each mouse was exposed to the open field at least once per day and not more than twice per day (once in the morning and once in the afternoon, session separated by at least 3 hr). All mice had significant exposure to both box types, when both were used. Before and after each session, the mice rested in their home cage in the mouse housing room. The floor of the test box was cleaned with soapy water between each trial.

Spike Sorting and Cell Classification

Putative excitatory cells were distinguished from putative interneurons using a combination of spike width and average rate. Due to the importance of dorsal-ventral location for grid scale, atypical waveforms suggestive of axons were also distinguished and were not used in any analysis (n = 25). Only cells with a total of more than 100 spikes were used in analyses.

Position Estimate

Position estimates were based on tracking of the LEDs on the head stage connected to the microdrive. All data was speed filtered and only epochs with instantaneous running speeds of 2.5 cm/s or more were included. Firing rate distributions were determined for trials with more than 80% coverage in the 50 cm box and 70% coverage in the 100 cm box by counting the number of spikes in each bin as well as the time spent per bin.

Identification and Characterization of Cell Types

Consistent with previous research, we observed grid cells in medial entorhinal cortex of mice (Fyhn et al., 2008). Spatial autocorrelation analysis confirmed the regularity and hexagonal pattern of grid fields. To quantify hexagonal periodicity we computed a grid score for each cell by taking a circular sample of the autocorrelation and comparing rotated versions of this sample. The Pearson correlation of this circle, with its rotation in alpha degrees, was obtained for angles of 60 degrees and 120 degrees and for 30, 90

and 150 degrees (Sargolini et al., 2006). The cell's grid score was defined as the minimum difference between any of the elements in the first group and any elements of the second. Grid spacing was defined as the median distance between the center and the nearest six peaks in the autocorrelogram. Grid spacing was analyzed only for cells where the median distance to the six nearest peaks matched the radius of the circle that gave the highest grid score (the 'outer radius' OR). When the ratio between these two measures was beyond 2 standard deviations of the mean (mean ratio 1.26, standard deviation 0.32), the cell was excluded (7 out of 134 cells). Grid field size was defined as the radius of the circle around the center field of the autocorrelation map, referred to as the 'inner radius' (IR). We identified border cells by computing, for each cell, the difference between the maximal length of a wall touching on a single firing field and the average distance of the firing locations from the nearest wall, dividing by the sum of those values. To identify head direction cells, the directional modulation of each individual cell was quantified by computing the length of the mean vector (the Rayleigh vector) for the distribution of firing rates across all head directions.

Shuffling Procedure for Grid Scores

Grid cells were defined as cells in which rotational symmetry-based grid scores exceeded the 99th percentile of a distribution of grid scores for shuffled recordings from the entire population of cells in the same age group and the same brain region. Shuffling was performed in the same way as by Langston et al. (2010). The chance level was determined for each group and layer by a random permutation procedure using all cells recorded in that group, layer and box. One hundred permutations were performed for each cell in the sample. For each permutation trial, the entire sequence of spikes fired by the cell was time-shifted along the animal's path by a random interval between 20 s and the total trial length minus 20 s, with the end of the trial wrapped to the beginning. The shuffling procedure was repeated 100 times for each of the cells in the sample. For each permutation, a firing rate map and an autocorrelation map were constructed and a grid score was calculated. The 99th percentile was read out from the overall distribution of grid scores in the shuffled data for each region. A cell was defined as a grid cell when the grid score exceeded this 99th percentile. The probability of obtaining the observed number of grid cells by chance was estimated for each sample with a binomial test (expected probability P_o = 0.05). Shuffling procedures were conducted separately for each group (control versus KO), each region (layer II versus layer III), and each box size (100 cm versus 50 cm), yielding a total of eight shuffled values in the 99th percentile for each cell type.

Speed Analysis of the Interspike Interval and Theta Frequency

For the analysis of theta frequency, an acausal (zero phase shifted), frequency domain, finite impulse response bandpass filter was applied to the signals. For theta filtering, 4 and 5 Hz were chosen for the stopband and passband, respectively, for the low cut-off frequencies; 10 and 11 were chosen for the passband and stopband high cut-off frequencies. To analyze the speed modulation of theta frequency, the peaks of the filtered theta signal were detected and the frequency determined on a cycle by cycle basis. Position samples were used to determine the instantaneous speed for 20 ms time bins. To quantify the relationship between theta frequency and speed, data was pooled for portions of the trial corresponding to speeds between 2.5 cm/s and 50 cm/s. A regression line was fit to the data and the slope of this line is reported. For the analysis of the inter spike interval, the same instantaneous speeds were used and the data pooled according to speed bins of 10 cm/s. An autocorrelation was constructed for each speed bin and the second peak measured.

Simulations Using the Burgess Model

For the simulations presented here, data on subthreshold oscillations was used from Giocomo and Hasselmo (2009). Simulations were run in MATLAB directly from m files. The MATLAB scripts were adapted from scripts written by Michael Hasselmo and Eric Zilli (Giocomo and Hasselmo, 2008a; Giocomo et al., 2007; Hasselmo et al., 2007). Previous research from rats indicated that grid spacing and the frequency of subthreshold oscillations can be scaled to relate systematically to one another (Giocomo et al., 2007). A scale function H(z) can be used such that H(z)/f(z) = G(z), where f is the frequency of subthreshold oscillations and G is the spacing of grid cells in vivo. For simulations presented here, H was re-calculated using membrane potential oscillation data collected from adult mice in Giocomo and Hasselmo (2009) and the in vivo grid spacing from control mice presented in this paper. For all simulations, we assume H is a constant and use the average H value calculated from data located 0 to 1,500 μm from the dorsal border of MEC (215 Hz cm). See Giocomo et al. (2007) for details about computing H from biological data. For simulations of grid spacing, the membrane potential oscillation frequencies measured in Giocomo and Hasselmo (2009) were used.

Simulations and Predictions of Oscillatory Inference Models

Oscillatory interference models of grid cells use changes in the frequency of oscillators to translate information about the speed and direction of the animal into a periodic grid pattern. We examined the implications of the observed increase in grid spacing in HCN1 knockout mice for two oscillatory interference models (Giocomo et al., 2007 and Burgess, 2008; Jeewajee et al., 2008). The first version we examined uses the absolute frequency of intrinsic oscillations to scale grid cell spacing along the dorsal-ventral axis (Giocomo et al., 2007). The second version we examined uses the amount of change in the frequency of intrinsic oscillations to movement related input to scale grid cell spacing along the dorsal-ventral axis (Burgess et al., 2007; Burgess, 2008).

First, the 'multiplicative version' of the single cell oscillatory interference model uses the resonant or oscillation frequency to directly translate between the temporal oscillatory properties of the neuron and the measured grid cell spacing. We performed

simulations of the 'multiplicative version' of the oscillatory interference model described in Giocomo et al., 2007 and adapted from scripts written by Michael Hasselmo and Eric Zilli (Giocomo et al., 2007; Giocomo and Hasselmo, 2008a). The frequency of membrane potential oscillations recorded in vitro (Giocomo & Hasselmo, 2009) was used to determine the predicted spacing of grid cells in vivo using the oscillatory interference model.

Second, we examined the originally proposed oscillatory interference model (Burgess et al., 2007; Burgess, 2008) which assumes that grid spacing depends on the amount of change in the intrinsic frequency of a single neuron to input about the speed and direction the animal is traveling. This version of the model makes specific predictions about the relationships between the global theta frequency, the intrinsic firing properties (ISI) and grid spacing (See Jeewajee et al., 2008 for a detailed derivation of these predictions). This model predicts that in control mice the frequency of the EEG-measured theta rhythm should depend on running speed and the slope of this relationship (Hz/cm/s) will be reduced in HCN1 knockout mice. This model also predicts a specific relationship between the firing rate frequency (fi), the theta rhythm while the animal is stationary (f0), the average running speed of the animal (s(t)) and the spacing of the grid cell (G) (Jeewajee et al., 2008). This relationship is detailed in the following equation:

$$\langle f_i(t)\rangle = f_0 + \frac{2(\pi+1)}{\sqrt{3\pi G}}\, s(t)$$

We used this equation to examine if the increase in grid spacing and inter spike interval observed with the loss of HCN1 followed the relationship predicted by this model. First, we calculated the measured interspike interval for three different speed bins (slow: 0-10 cm/s; medium: 10-20 cm/s; fast: 20-30 cm/s). The parameter s(t) for each speed bin was estimated as: 5 cm/s; 15 cm/s and 25 cm/s respectively. Only the subset of grid cells presented in Figure 2B were used in this analysis as any errors in the parameter G will introduce variability in the predicted measure fi.

SUPPLEMENTAL REFERENCES

Burgess, N. (2008). Grid cells and theta as oscillatory interference: theory and predictions. Hippocampus *18*, 1157–1174.

Fyhn, M., Hafting, T., Witter, M.P., Moser, E.I., and Moser, M.B. (2008). Grid cells in mice. Hippocampus 18, 1230–1238.

Garden, D.L., Dodson, P.D., O'Donnell, C., White, M.D., and Nolan, M.F. (2008). Tuning of synaptic integration in the medial entorhinal cortex to the organization of grid cell firing fields. Neuron *60*, 875–889.

Giocomo, L.M., and Hasselmo, M.E. (2008a). Computation by oscillations: implications of experimental data for theoretical models of grid cells. Hippocampus *18*, 1186–1199.

Giocomo, L.M., and Hasselmo, M.E. (2009). Knock-out of HCN1 subunit flattens dorsal-ventral frequency gradient of medial entorhinal neurons in adult mice. J. Neurosci. *29*, 7625–7630.

Giocomo, L.M., Zilli, E.A., Fransén, E., and Hasselmo, M.E. (2007). Temporal frequency of subthreshold oscillations scales with entorhinal grid cell field spacing. Science *315*, 1719–1722.

Hafting, T., Fyhn, M., Molden, S., Moser, M.B., and Moser, E.I. (2005). Microstructure of a spatial map in the entorhinal cortex. Nature *436*, 801–806.

Hasselmo, M.E., Giocomo, L.M., and Zilli, E.A. (2007). Grid cell firing may arise from interference of theta frequency membrane potential oscillations in single neurons. Hippocampus *17*, 1252–1271.

Jeewajee, A., Barry, C., O'Keefe, J., and Burgess, N. (2008). Grid cells and theta as oscillatory interference: electrophysiological data from freely moving rats. Hippocampus *18*, 1175–1185.

Langston, R.F., Ainge, J.A., Couey, J.J., Canto, C.B., Bjerknes, T.L., Witter, M.P., Moser, E.I., and Moser, M.B. (2010). Development of the spatial representation system in the rat. Science *328*, 1576–1580.

Nolan, M.F., Malleret, G., Lee, K.H., Gibbs, E., Dudman, J.T., Santoro, B., Yin, D., Thompson, R.F., Siegelbaum, S.A., Kandel, E.R., and Morozov, A. (2003). The hyperpolarization-activated HCN1 channel is important for motor learning and neuronal integration by cerebellar Purkinje cells. Cell *115*, 551–564.

Sargolini, F., Fyhn, M., Hafting, T., McNaughton, B.L., Witter, M.P., Moser, M.B., and Moser, E.I. (2006). Conjunctive representation of position, direction, and velocity in entorhinal cortex. Science *312*, 758–762.

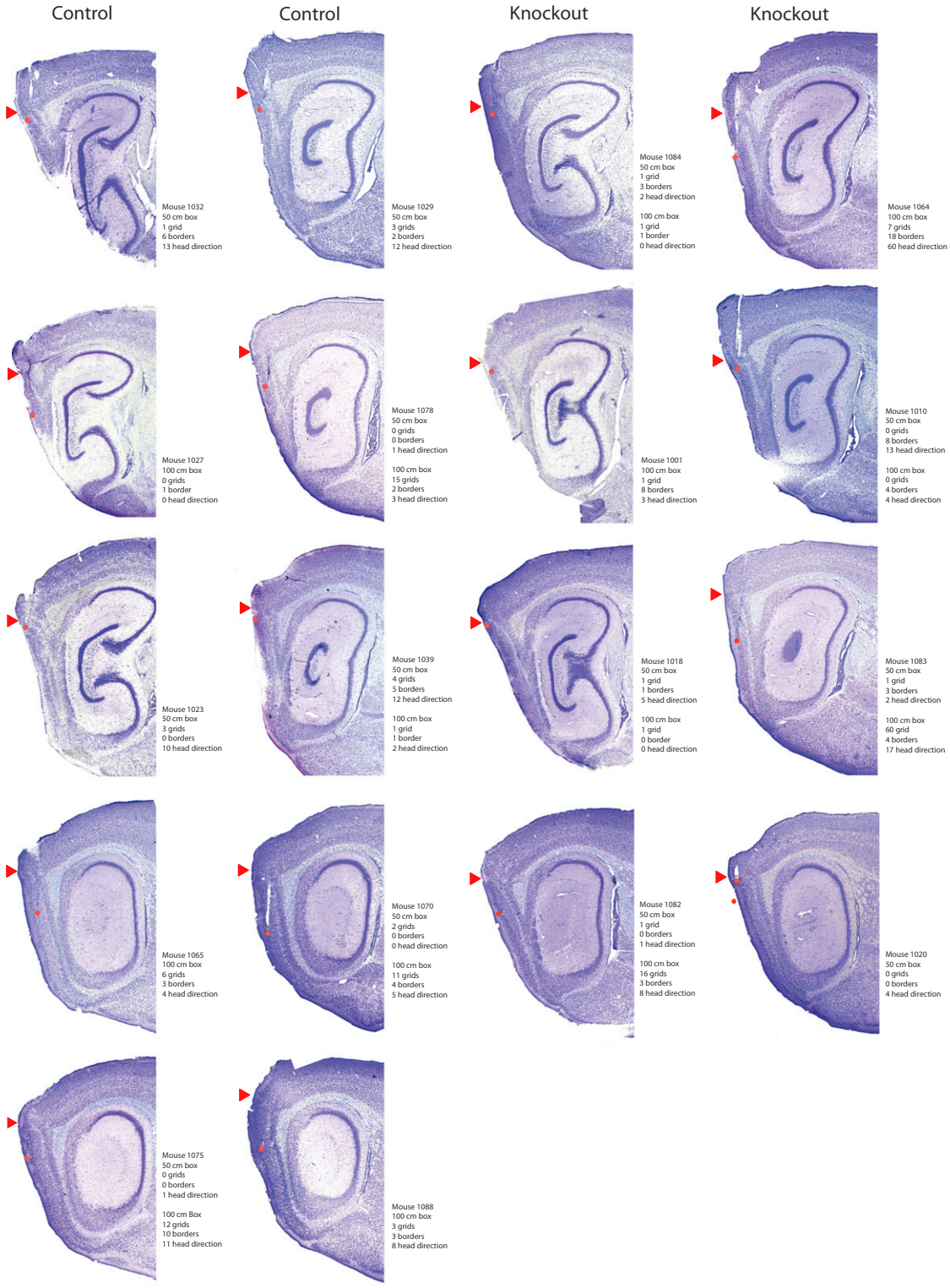

Figure S1. Histology for All Mice with Recordings in Layer II/III of MEC, Related to Figure 3

Left two columns: Control mice; Right two columns: HCN1 knockout mice. Sagittal images are presented from most medial to most lateral recording location. Red dot marks the deepest tetrode location. Red arrow marks the dorsal border of MEC. Number of grid cells, border cells and head direction cells recorded in each environment is indicated to the right of each image. Mean distances from the dorsal border of MEC in the 100 cm box ± SEM: Control = 702 ± 10 μm, range = 1100 μm; KO = 609 ± 16 μm, range = 1000 μm. In the 50 cm box ± SEM: Control = 192 ± 11 μm, range = 750 μm; KO = 225 ± 29 μm, range = 875 μm.

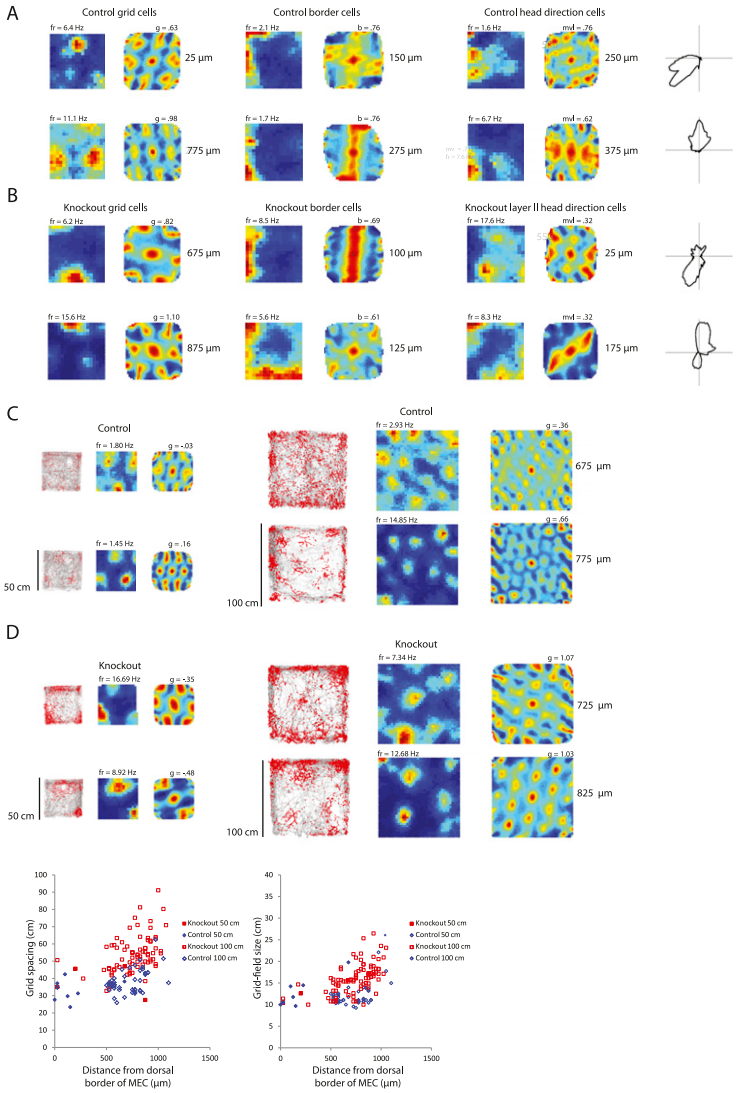

Figure S2. Entorhinal Cell Types Recorded in the 50 cm Box, Related to Figure 6

(A and B) Examples of grid cells, border cells and head direction cells. In the 50 cm box both control (A) and KO mice (B) had grid cells (Control mice 4.7%; KO mice 4.0%), border cells (Control mice 6.1%; KO mice 16.8%) and head direction cells (Control mice 27.8%; KO mice 45.5%). Two examples of each cell type from each group (control and KO) are shown. Rate maps (left in each column) and autocorrelation maps (right in each column) are color-coded, to show minimum (dark blue) and maximum (red) values. The scale of the autocorrelation diagrams is twice the scale of the rate maps. The directional plots show firing rate as a function of head direction (far right). Maximum firing rate (fr), grid scores (g), border scores (b) and mean vector length (mvl) are provided for each cell at the top of the plots. Distance from the entorhinal border is marked on the right of each autocorrelation plot. The number of grid, border and head direction cells in layer II and III was significantly larger than expected by random selection from the shuffled distributions for cells in the 50 cm box in both groups (Control: Grids layer II, $Z = 3.00$, $p < 0.01$; Grids layer III, $Z = 4.54$, $p < 0.001$; Borders layer II, $Z = 4.31$, $p < 0.001$; Borders layer III, $Z = 6.15$, $p < 0.001$; Head Direction layer II, $Z = 33.85$, $p < 0.001$; Head Direction layer III, $Z = 20.09$, $p < 0.001$; KO mice: Grids layer II, $Z = 2.1$, $p = 0.04$; Grids layer III, $Z = 2.13$, $p = 0.03$; Borders layer II, $Z = 7.73$, $p < 0.001$; Borders layer III, $Z = 14.92$, $p < 0.001$; Head Direction layer II, $Z = 22.85$, $p < 0.001$; Head Direction layer III, $Z = 24.92$, $p < 0.001$). Criteria determined from randomly shuffled data including all cells from the respective layer for the 50 cm box were as follows: Control, layer II and III respectively, grid score = .49 and .46; border score = .57 and .57; mean vector length = .23 and .21 and KO, layer II and III respectively, grid score = .49 and .51; border score = .57 and .55; mean vector length = .17 and .18.

(C and D) Comparison of grid cells in the 50 cm box (left) and 100 cm box (right). Control cells are shown in C and HCN1 KO cells shown in D. Grids showed one to several peaks in the 50 cm box (left), but too few to determine for each cell if the cell was periodic, resulting in a poor grid score and inaccurate spacing measure. In the 100 cm box grids showed multiple peaks for the anatomical range that we covered, allowing a more accurate spacing measure. Left, in each panel, trajectory (gray) with firing locations superimposed (red). Each red dot represents a single spike. Middle and right in each panel, rate maps (middle) and autocorrelation maps (right) color-coded for minimum (dark blue) and maximum (red) values. Symbols as in part A and B.

(E and F) Scatterplots showing grid spacing (E) and grid field size (F) for all control and KO cells in the 50 cm box. Grid spacing was defined as the median distance between the center and the nearest six peaks in the autocorrelogram. Grid field size was defined as the radius of the circle around the center field of the autocorrelation map, referred to as the 'inner radius' (IR).

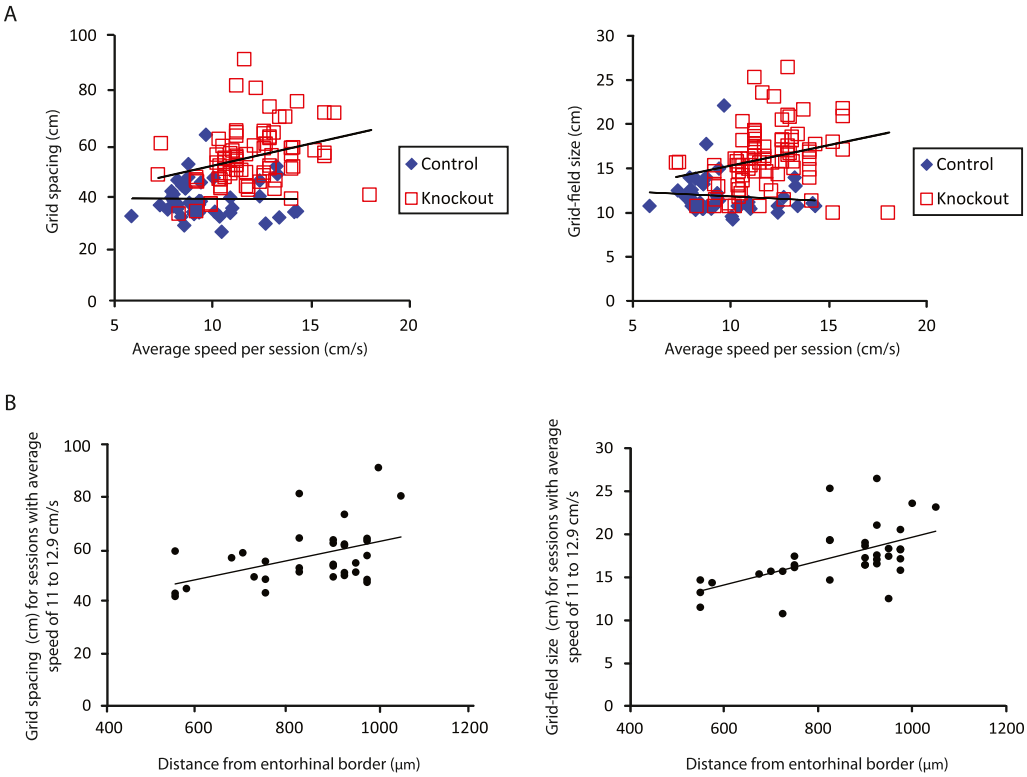

Figure S3. Speed Did Not Affect the Group Difference in Grid Spacing, Related to Figure 2

(A) Scatterplots show grid spacing (left) and grid field size (right) as a function of running speed. On average, KO mice ran slightly faster than control mice in the 100 cm box (11.84 ± .21 cm/s and 9.56 ± 2.79 cm/s, respectively; $t(132) = 6.47$, $p < 0.001$). Even so, KO mice still showed significantly higher grid spacing and grid field size, compared to controls at all overlapping speeds. When a regression line was fit to the scatterplots for each group, the regression lines for both grid spacing and grid field size had a higher Y-intercept in HCN1 KO compared to control mice (grid field size: $F(1,130) = 34.67$, $p < 0.001$, $\eta 2 = .21$; grid spacing: $F(1,124) = 44.29$ $p < 0.001$, $\eta 2 = .26$), indicating a difference in grid scale regardless of speed differences.

(B) Scatterplots showing that speed did not affect the preservation of a gradient in grid spacing in HCN1 KO mice. Grid spacing (left) and grid field size (right) was plotted relative to dorsal-ventral recording position for the speed bin encompassing the largest number of grid cells (11 to 12.9 cm/s). For this speed bin, HCN1 KO mice still showed a significant gradient (grid spacing: $r(31) = .45$ $p < 0.01$; grid field size: $r(34) = .56$ $p < 0.001$).

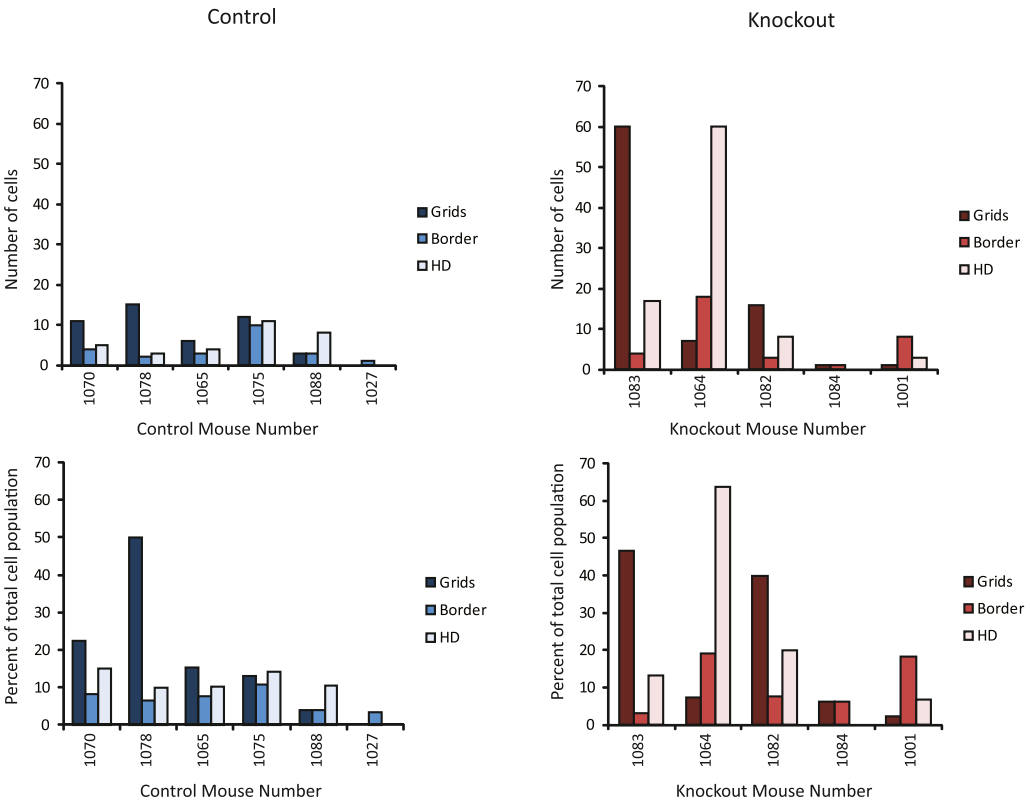

Figure S4. Proportions of Cell Type for Control and Knockout Mice, Related to Figure 7

Individual control (left) and KO mice (right) showed different proportions of grid cells, border cells and head direction cells, most likely due to slightly different coordinates sampling clusters of particular cell types. The number of each cell type (top) and the percent of each cell type compared to the total cell population (bottom) are shown for the six control mice (left) and five KO mice (right) that had at least twenty individual MEC cells in the 100 cm box. There was no significant difference in the percentage of grid cells observed in KO and control animals (20.5 ± 9.1% and 17.5 ± 7.3%, respectively, averaged across animals; $t(9) = .26$, $p = 0.80$). In addition, there was no significant difference in the percentage of border cells or head direction cells (Borders: 10.8 ± 3.2% and 6.8 ± 1.1%, respectively, averaged across animals, $t(9) = 1.26$, $p = 0.24$; Head direction: 20.8 ± 9.8% and 10.0 ± 2.2, respectively, averaged across animals, $t(9) = 1.03$, $p = 0.33$).

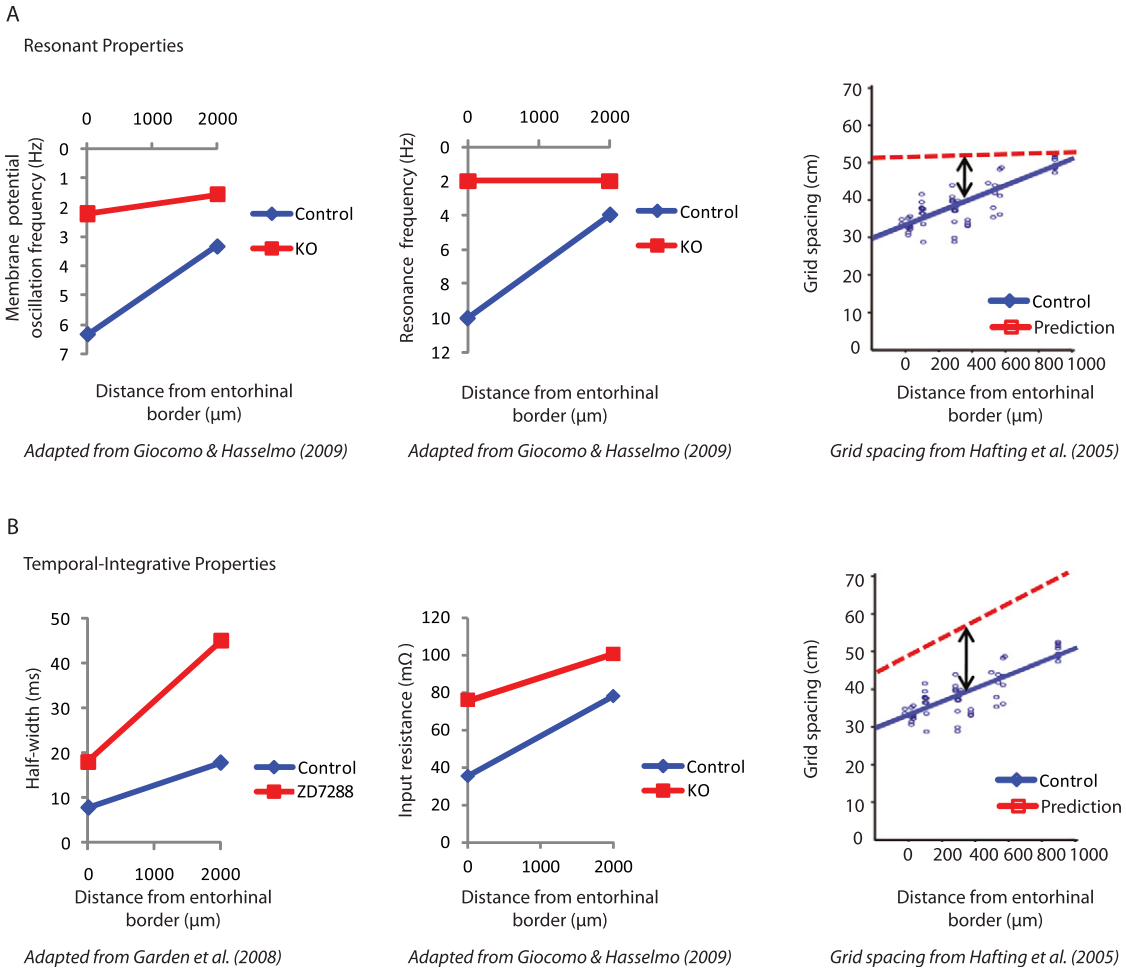

Figure S5. Comparison of In Vitro and In Vivo Dorsal-Ventral Gradients in MEC, Related to Figure 4

(A) Changes in dorsal-ventral properties of in vitro membrane potential oscillation frequency (far left) and resonant frequency (middle) with KO of HCN1. Knockout of HCN1 significantly reduces the slope in resonant properties compared to control animals. If h current-dependent resonant properties exclusively determined the grid spacing gradient, we would predict that HCN1 KO mice would show a flatter dorsal-ventral gradient in grid spacing (slope) in vivo (far right). Left and middle plot adapted from Giocomo and Hasselmo (2009). Far right plot reprinted and adapted from Hafting et al. (2005).

(B) Changes in dorsal-ventral properties of the excitatory post-synaptic potential (EPSP) half-width (far left) and input resistance (middle) with pharmacological block of Ih or KO of HCN1, respectively. Reduction of Ih significantly shifts the gradient along the *y* axis (Δ Y), but a gradient is still clearly present. If h current-dependent temporal-integrative properties determined grid scale and the grid spacing gradient, we would predict HCN1 KO mice would show a shift in grid scale along the dorsal-ventral axis with a preserved gradient (Δ Y) in vivo (far right). The change in grid spacing we observed in vivo with loss of HCN1 best matches the change seen in temporal-integrative properties with loss of HCN1 in vitro. Left plot adapted from Garden et al. (2008). Middle plot adapted from Giocomo and Hasselmo (2009). Far right plot reprinted and adapted from Hafting et al. (2005).

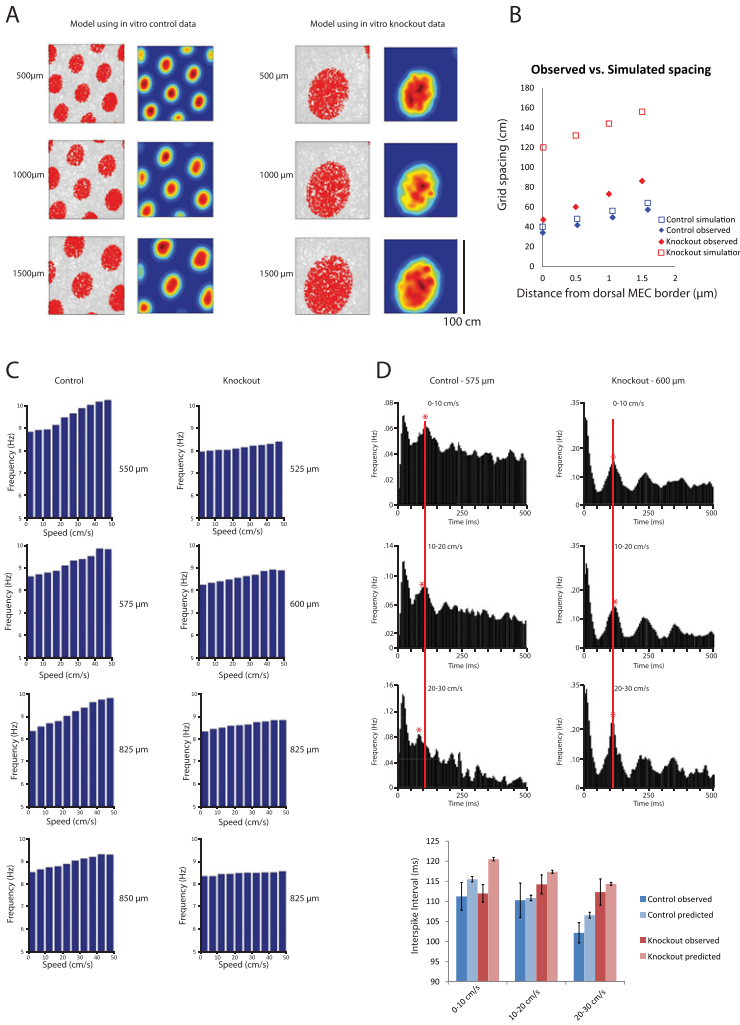

Figure S6. Simulations and Predictions of Oscillatory Inference Models, Related to Figure 5

(A and B) Simulations of the oscillatory interference model (Giocomo et al., 2007).

(A) Simulations of grid spacing along the dorsal-ventral axis in control mice (left two columns) and knockout mice (right two columns), based on the dorsal-ventral gradient in membrane potential oscillation frequency observed in normal mice in vitro. Left: Trajectory with spike positions. Right: Color coded rate maps.

(B) Grid spacing as a function of dorsal-ventral position in MEC. Unfilled squares represent the predicted dorsal-ventral gradient in grid spacing based on simulations (part A). Filled diamonds represent the linear fit to the observed dorsal-ventral gradient in grid spacing in vivo for control and HCN1 KO mice. Note that for the HCN1 knockout mice, grid spacing is much larger in the simulations than in the observed data. These simulations, combined with the preserved gradient in grid scale with loss of HCN1, suggest that the absolute frequency of h current-dependent resonance does not independently determine grid spacing.

(C and D) Experimental predictions of the oscillatory interference model (Burgess, 2008). This model predicts that in control mice the frequency of the EEG-measured theta rhythm should depend on running speed and the slope of this relationship (Hz/cm/s) will be reduced in HCN1 knockout mice.

(C) As presented in the main text, we found a positive correlation between running speed and theta frequency in control animals (0.02 ± .002 Hz/cm/s) and a significant reduction in the slope of this correlation in knockout animals (.008 ± .001 Hz/cm/s). Examples of the theta frequency relative to running speed are plotted for four individual control animals and three individual knockout animals. For the knockout animals, the same animal is presented at two different depths (the top and bottom plot). Depth for each measurement is located to the right of each plot.

(D and E) This model also predicts a specific relationship between the firing rate frequency (fi), the theta rhythm while the animal is stationary (f0), the average running speed of the animal (s(t)) and the spacing of the grid cell (G) (Jeewajee et al., 2008). For this analysis, the average size of grids in the control group was 41.9 ± 1.1 cm (n = 16) and 69.9 ± 2.0 cm (n = 30) in the knockout group. We examined the predicted inter spike interval by converting the predicted intrinsic frequency values (1000/predicted intrinsic frequency = predicted inter spike interval). As determined by a repeated-measures ANOVA, the predicted and measured inter spike interval was not significantly different for the control group ($F(1,15) = 2.37$, $p = 0.15$, $\eta 2 = .14$). There was a significant difference between the predicted and measured inter spike intervals for the knockout group ($F(1, 29) = 8.78$, $p = 0.006$, $\eta 2 = .23$) but this most likely reflected the reduction in speed modulation of the inter spike interval. An individual example of the inter spike interval at three speed bins from a control mouse (575 µm deep) and knockout mouse (600 µm deep) are shown in D. The measured and predicted inter spike intervals for all grid cells analyzed are shown in E. Error bars represent ± SEM. The overall reduction in the modulation of the inter spike interval and theta frequency by speed is consistent with the predictions of the originally proposed oscillatory interference model (Burgess et al., 2007; Burgess, 2008). However, the degree to which this in vivo reduction in the speed modulation of theta and intrinsic frequencies match the predicted grid spacing by this version of the oscillatory interference model should be examined in future iterations of computational models.

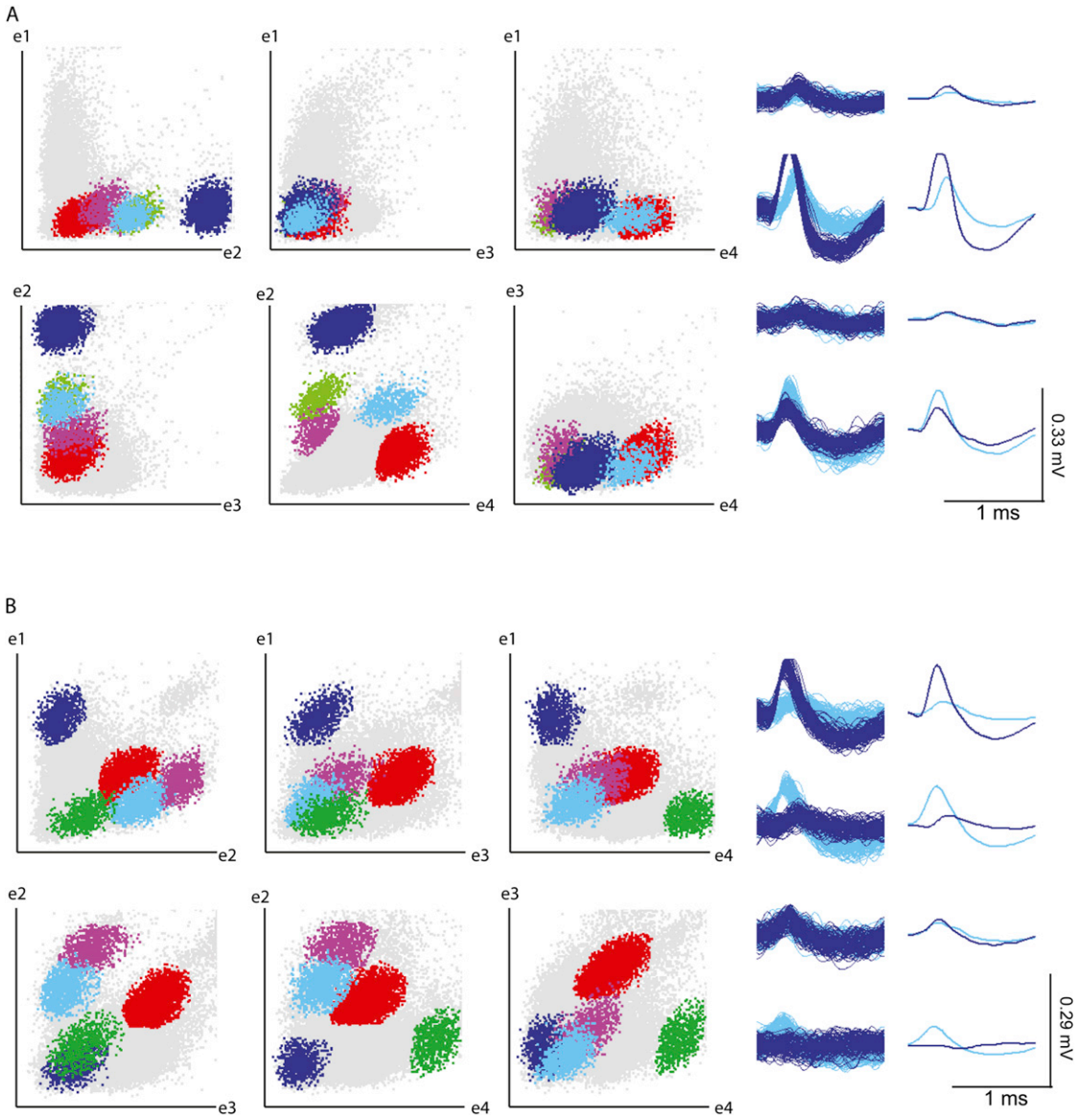

Figure S7. Cluster Diagrams and Waveforms for a Control Mouse and a Knockout Mouse, Related to Figure 1

Scatterplots (left) showing the relationship between peak to trough amplitudes for all signals recorded on each pair of electrodes on a given tetrode. Each dot represents a single sampled spike. Waveforms (right) are shown for each of the four electrodes (e1-e4) of the tetrode. All cells shown are principal neurons according to their waveforms and firing rates. The examples show that the separation of clusters and waveforms in MEC was qualitatively similar in control and KO mice. This was confirmed in quantitative analyses of cluster separation in the total cell sample. Cluster separation was estimated by calculating distances between cluster spikes of different cells (isolation distances) in Mahalonobis space. Median Mahalonobis distances were 13.3 for control mice and 12.9 for HCN1 KO mice. There was no significant difference between control and HCN1 KO clusters in MEC ($Z = .28$, $p = 0.78$, Wilcoxon rank-sum test).